

# Valley-Polarized State Induced $\varphi_0$ -Josephson Junction in Twisted Bilayer Graphene

Ying-Ming Xie,<sup>1,\*</sup> Dmitri K. Efetov,<sup>2</sup> and K. T. Law<sup>1,†</sup>

<sup>1</sup>*Department of Physics, Hong Kong University of Science and Technology,  
Clear Water Water Bay, 999077 Hong Kong, China*

<sup>2</sup>*ICFO - Institut de Ciències Fotoniques, The Barcelona Institute  
of Science and Technology, Castelldefels, Barcelona, 08860, Spain*

(Dated: February 14, 2022)

Recently, gate-defined Josephson junctions in magic angle twisted bilayer graphene (MATBG) were studied experimentally and highly unconventional Fraunhofer patterns were observed. In this work, we show that an interaction-driven valley-polarized state connecting two superconducting regions of MATBG would give rise to a long-sought-after purely electric controlled  $\varphi_0$ -junction in which the two superconductors acquire a finite phase difference  $\varphi_0$  in the ground state. We point out that the emergence of the  $\varphi_0$ -junction stems from the time-reversal symmetry breaking valley polarization and an intravalley inversion symmetry breaking term. Importantly, a spatially non-uniform valley polarization order parameter at the junction can explain the highly unconventional Fraunhofer patterns observed in the experiment. Our work explores the novel transport properties of the valley-polarized state and suggests that gate-defined MATBG Josephson junctions could realize the first purely electric controlled  $\varphi_0$ -junctions with applications in superconducting devices.

*Introduction.*—The discovery of correlated insulating states and superconducting states in magic angle twisted bilayer graphene (MATBG) [1–3] motivated intense studies of moiré materials in recent years. The rich symmetry breaking states discovered in MATBG [4–37] enable the creation of novel quantum devices with various quantum phases on a single material platform. Recently, gate-defined Josephson junctions (JJs) were created on MATBG [38–41] when a non-superconducting (weak-link) region in a superconducting MATBG device was created by local gating. Interestingly, a highly unconventional Fraunhofer pattern was observed in Ref. [40] when the weak-link region was gated to near half-filling  $\nu = -1/2$  filling (with two holes per moiré unit cell). Among other features, the Fraunhofer pattern showed a shift of central peak away from the zero magnetic field, a high level of asymmetry with respect to the central peak, and a non-vanishing critical supercurrent for a wide range of magnetic fields. Such Fraunhofer patterns clearly indicate the appearance of a time-reversal symmetry breaking state at the junction [40]. As conventional Fraunhofer patterns were observed once the junction region is gated away from  $\nu = -1/2$  filling without changing the superconducting part of the junction, it would suggest that the time-reversal symmetry comes from the weak-link region at half-filling.

The observed unconventional Fraunhofer pattern motivated us to study the Josephson effects in a gate-defined superconductor/valley-polarized state/superconductor (SC/VP/SC) in MATBG, as schematically shown in Fig. 1(a). The valley-polarized state, in which the moiré bands of the K and -K valleys acquire a valley degeneracy breaking order parameter due to electron-electron

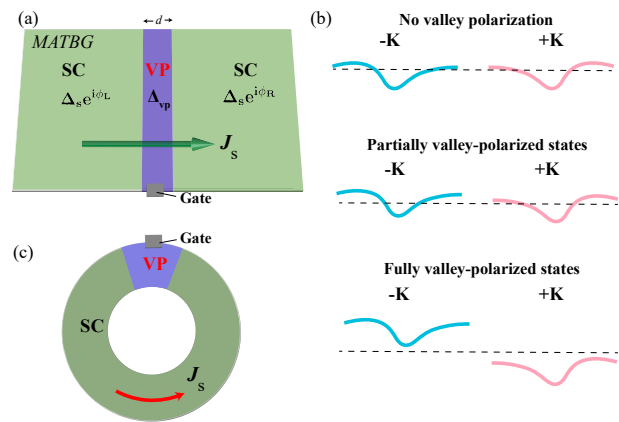


FIG. 1: (a) A schematic plot of a gate-defined MATBG Josephson junction. The left (right) side of the junction is superconducting with pairing order parameter  $\Delta_s e^{i\phi_L(R)}$ . The weak-link region has width  $d$  and a valley polarization order parameter  $\Delta_{vp}$ . (b) Illustrations of the moiré bands at  $K$  and  $-K$  valleys which are not valley polarized, partially valley-polarized, and fully valley-polarized, respectively [31, 42]. The black dashed lines denote the Fermi levels. (c) A schematic plot of a MATBG superconducting ring with a region gated into the valley-polarized state. The  $J_s$  (red arrow) represents a spontaneous supercurrent.

interactions [see the illustration in Fig. 1(b)], is taken as the natural candidate for a time-reversal symmetry breaking state at half-filling [28–36, 42]. The valley-polarized state, such as the valley-polarized quantum anomalous Hall state [18, 19], is a new state of matter whose novel properties have yet to be much explored. In this work, we show that the current-phase relation induced by the interaction-driven valley-polarized state as the weak link of a Josephson junction is highly unconventional, which has the form  $I_s = I_c \sin(\phi - \varphi_0)$ . Here,  $I_c$  is the critical current,  $\phi = \phi_L - \phi_R$  is the phase

\*ymxie@ust.hk

†phlaw@ust.hk

difference of the two superconductors with phases  $\phi_L$  and  $\phi_R$  respectively. Importantly,  $\varphi_0$ , which depends on the junction parameters, generally varies from 0 to  $2\pi$ . Such Josephson junctions with general  $\varphi_0$  are called  $\varphi_0$ -Josephson junctions ( $\varphi_0$ -JJs). In this work, we point out that the valley polarization and the trigonal warping effects, which break the intravalley inversion symmetry of moiré bands, are the key ingredients for realizing  $\varphi_0$ -JJs. Importantly, a spatially non-uniform valley polarization order parameter at the junction can naturally explain the unconventional Fraunhofer patterns observed in the experiment [40].

$\varphi_0$ -JJs have important potential device applications, such as superconducting spintronics [43, 44], Josephson qubits [45–47], and phase batteries [48]. The previously proposed realizations of  $\varphi_0$ -JJs involve ferromagnetic materials [49–59] or materials with spin-orbit coupling [60–70] (such as semiconducting nanowire and topological insulators). However, experimentally realizations of  $\varphi_0$ -JJ were rare and the presence of external magnetic fields was needed [68–70]. Our work establishes a new mechanism to create  $\varphi_0$ -JJs, which does not rely on either ferromagnetism or spin-orbit couplings. More importantly, the gate-defined  $\varphi_0$ -JJs created with MATBG are interaction-driven and the junction properties can be controlled by pure electric gating.

*Model.*—Here, we first introduce a microscopic model which captures the key ingredients of a MATBG Josephson junction as realized experimentally in Ref. [40] and schematically shown in Fig. 1(a). We capture the relevant moiré bands near charge neutrality of MATBG with an effective two-orbital tight-binding model on a hexagonal lattice according to Ref. [4, 5], which can be written as :

$$H_0 = \sum_{\langle ij \rangle, \xi} t_1 c_{i\xi}^\dagger c_{j\xi} + \sum_{\langle ij \rangle', \xi} t_{2\xi} c_{i\xi}^\dagger c_{j\xi} + \text{H.c.} - \sum_{i, \xi} \mu_i c_{i\xi}^\dagger c_{i\xi}. \quad (1)$$

Here,  $\xi$  labels the two  $p$ -wave-like orbitals  $p_x + i\xi p_y$  as a representation of two valleys  $\tau = \pm K$ ,  $t_1 = 0.331$  meV and  $t_{2\xi} = -0.01 + 0.097\xi i$  meV denote the first-nearest neighbor and the fifth-nearest neighbor hopping. Note that the imaginary part of  $t_{2\xi}$  describes the warping effects. Moreover, the spatial dependent chemical potential is denoted by  $\mu$  which is chosen such that the filling factor  $\nu$  satisfies  $-1 < \nu < -1/2$  for the superconducting part of the junction and  $\nu \approx -1/2$  at the weak-link region [40]. As shown in Ref. [4, 5],  $H_0$  captures the symmetries of the moiré bands of MATBG.

We next include the effects of interactions through a mean-field consideration. Specifically, we introduce the superconducting order parameter on the left (L) and right (R) sides of the Josephson junction and the valley polarization order parameter to the weak link. The resulting effective tight-binding Hamiltonian is:

$$H_{\text{eff}} = H_0 + \sum_{i \in (L, R), \xi} (\Delta_s e^{i\phi_{L(R)}} c_{i\xi}^\dagger c_{i-\xi}^\dagger + \text{H.c.}) + \sum_{i \in \text{WL}, \xi} \Delta_{\text{vp}} c_{i\xi}^\dagger (\tau_z)_{\xi\xi'} c_{i\xi'}. \quad (2)$$

Here, the second term characterizes the pairing potential on the left and right side of the Josephson junction with phases  $\phi_L$  and  $\phi_R$  respectively. Without loss of generality, we set the spin-singlet pairing [10, 71] amplitude  $\Delta_s$  to be a constant  $0.1W_b$ , where  $W_b$  is the moiré band width [3, 40]. It is important to note that other time-reversal invariant unconventional pairings have been proposed in MATBG [37, 72]. However, as shown in the Supplementary Material (SM) [73], the unconventional Josephson effect mostly originates from the time-reversal symmetry breaking weak-link region and the conclusions obtained here are insensitive to the superconducting pairing symmetries. To take into account the temperature effects on the pairing strength, we set  $\Delta_s(T) = \Delta_s \tanh(1.74\sqrt{(T_c - T)/T})$  ( $T_c$  is the superconducting critical temperature) as described by the BCS theory [74].

On the other hand, the third term with the Pauli matrix  $\tau_z$  characterizes the valley polarization in the weak-link (WL) region with valley-polarization order parameter  $\Delta_{\text{vp}}$ . The order parameter  $\Delta_{\text{vp}}$  can be seen from the Hamiltonian with Coulomb interactions under the Hartree-Fock mean-field calculation [see SM [73]]. More details about the tight-binding model adopted in the calculation can be found in the SM [73].

*Unconventional Josephson junction induced by the valley-polarized state in MATBG.*—To study the properties of the gate-defined MATBG Josephson junction, we first calculate the energy dispersion as a function of phase difference  $\phi$  of the junction which is described by  $H_{\text{eff}}$ . To be specific, we set the length of the non-superconducting part of the junction be  $d = 10L_M$  [40] ( $L_M \approx 14$  nm is the moiré lattice constant), and set the filling  $\nu$  to be close to half-filling. To match the experimental situation in which the junction resistance is much smaller than the quantized resistance  $h/e^2$  [40], we set the weak-link regime to be partially valley-polarized [31, 42] such that the weak-link section is metallic as schematically illustrated in Fig. 1(b).

Figures 2. (a) and (b) show a typical energy spectrum of the MATBG Josephson junction as a function of the phase difference  $\phi = \phi_L - \phi_R$ , obtained by diagonalizing the junction Hamiltonian  $H_{\text{eff}}$  with  $\Delta_{\text{vp}}/\Delta_s = 0$  and  $\Delta_{\text{vp}}/\Delta_s = 1$ , respectively. As expected, there is a large number of Andreev bound states within the superconducting gap. The energy-phase relations of a few Andreev bound states with large slopes are highlighted by red solid lines in Figs. 2(a) and 2(b). It can be seen that the in-gap Andreev bound states with large slopes  $\frac{\partial E}{\partial \phi}$  contributing mostly to the supercurrent exhibit a phase shift which is close to (but not equal to)  $\pi$  when the valley polarization  $\Delta_{\text{vp}}/\Delta_s = 1$ . This phase shift gives the first indication that the valley polarization has nontrivial effects on the Josephson junction. The values of the phase shift will be also discussed in more details through an analytical analysis later. For the nearly flat in-gap bound states in Figs. 2 (a) and 2(b), they originate from the scattering states with large transverse momenta, con-

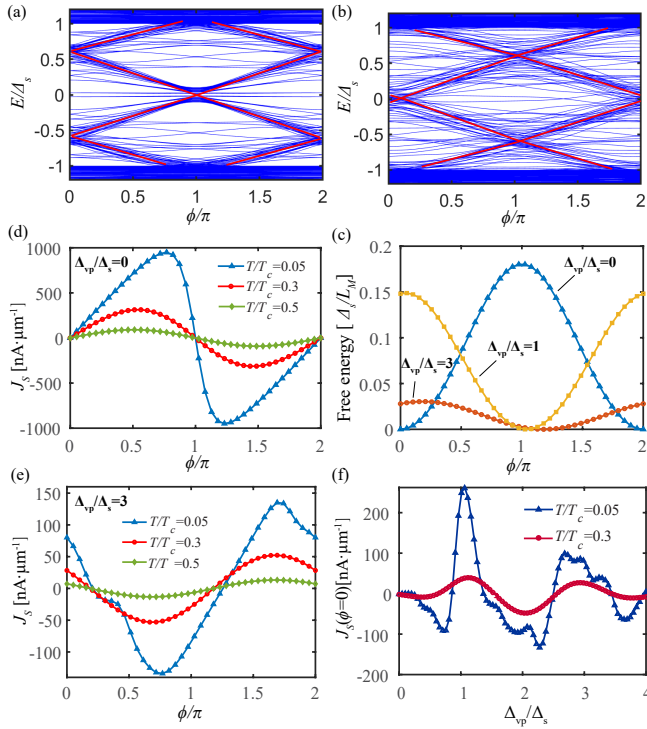


FIG. 2: (a) and (b) The energy levels of a MATBG Josephson junction versus the phase difference  $\phi$  in the cases of no valley polarization ( $\Delta_{vp}/\Delta_s = 0$ ) and with a valley polarization  $\Delta_{vp}/\Delta_s = 1$ , respectively, where red lines highlight the positions of Anreev bound states with large slopes. The width of the junction is  $W_J = 10\sqrt{3}L_M$  and length is  $d = 10L_M$ . The filling of weak-link region and the superconducting region are  $\nu \approx -0.5$  and  $\nu \approx -0.6$ , respectively. (c) The landscape of the free energy  $F_J(\phi)$  (in units of  $\Delta_s/L_M$ ) with  $\Delta_{vp}/\Delta_s = 0, 1, 3$ . The temperature is fixed at  $T/T_c = 0.3$ . (d) and (e) The supercurrent density (in the unit of  $\text{nA} \cdot \mu\text{m}^{-1}$ ) versus  $\phi$  at various temperatures in the cases of  $\Delta_{vp}/\Delta_s = 0$  and  $\Delta_{vp}/\Delta_s = 3$ , respectively. (f) The anomalous supercurrent  $J_s(\phi = 0)$  versus the valley polarization strength  $\Delta_{vp}$  at  $T/T_c = 0.05$  and  $T/T_c = 0.3$ .

tributing much less to the supercurrent.

To study the ground state of the Josephson junction, we calculate the free energy as  $F(\phi) = \int dr \frac{|\Delta_s|^2}{U} - k_B T \sum_n \ln(1 + e^{-E_n(\phi)/k_B T})$  [73], where  $U$  is an effective attractive interaction strength, and  $T$  is the temperature. We neglect the  $U$  dependent term which is independent of  $\phi$ . The energy of the states  $E_n(\phi)$  is obtained by diagonalizing the Hamiltonian  $H_{eff}(\phi)$ . For convenience sake, we define the free energy of the Josephson junction per unit width to be  $F_J(\phi) = W_J^{-1}(F(\phi) - \min[F(\phi)])$ , where  $W_J$  is the width of the junction. Therefore, the phase difference of the two superconductors at the ground state is determined by  $\phi_0$  such that  $F_J(\phi_0) = 0$ . In Fig. 2(c), we plot the free energy landscapes  $F_J(\phi)$  with temperature  $T = 0.3T_c$  at various valley polarization strengths ( $\Delta_{vp}/\Delta_s = 0, 1, 3$ ). As expected, without valley polarization, the junction is conventional so that the ground

state appears at  $\phi = 0$ . Interestingly, the ground state of the Josephson junction can appear at a finite  $\phi$  in the presence of valley polarization. For example, in the case of  $\Delta_{vp}/\Delta_s = 1$ , the ground state with  $F_J(\phi) = 0$  appears at a phase difference close to (but not equal to)  $\pi$ . For a larger  $\Delta$  such that  $\Delta_{vp}/\Delta_s = 3$ , the ground state appears at a phase further away from  $\pi$ .

To show the effect of valley polarization on the current-phase relation, the supercurrent density  $J_s$  (in unit of  $\text{nA} \cdot \mu\text{m}^{-1}$ ) as a function of  $\phi$  is depicted in Fig. 2(d) for the case without valley polarization ( $\Delta_{vp}/\Delta_s = 0$ ) and in Fig. 2(e) for the case with valley polarization ( $\Delta_{vp}/\Delta_s = 3$ ). Here, the supercurrent density is obtained from the free energy of the Josephson junction as  $J_s = \frac{2e}{\hbar} \frac{\partial F_J(\phi)}{\partial \phi}$ . Without valley polarization, the junction has conventional current-phase relation at both the low and high temperature regimes [75, 76]. However, in the case with finite valley polarization, the supercurrent can either exhibit a sign change or even display a generic phase shift [see Fig. 2(e)]. In particular, it can be seen that the curves with higher temperature [the red and green lines in Fig. 2(e)] follow a standard  $\varphi_0$ -JJ current-phase relation of  $J_s = J_c \sin(\phi - \varphi_0)$ . Our calculation thus clearly shows that the valley polarization can result in  $\varphi_0$ -JJs in MATBG.

One important consequence of a  $\varphi_0$ -JJ is that there is a supercurrent even at zero phase difference ( $\phi = 0$ ), called anomalous supercurrent [62, 63]. The anomalous supercurrent density  $J_s(\phi = 0)$  for  $\Delta_{vp}/\Delta_s = 3$  can be seen in Fig. 2(e). The  $J_s(\phi = 0)$  as a function of valley polarization strength  $\Delta_{vp}$  at various temperatures is shown in Fig. 2(f). We find that the anomalous supercurrent is generally finite with valley polarization. Moreover, when  $\Delta_{vp} \gg \Delta_s$ , the anomalous current density at the low temperature range can be as large as tens of  $\text{nA} \cdot \mu\text{m}^{-1}$ . As depicted in Fig. 1(c), we expect to see an anomalous current in a ring geometry when part of the superconducting ring is gated to the valley-polarized state. It is also important to note that unlike previously studied  $\varphi_0$ -JJs, the MATBG  $\varphi_0$ -JJs do not involve ferromagnetism or spin-orbit coupling, which calls for a new understanding about the underlying mechanism for the formation of  $\varphi_0$ -JJs in the MATBG.

*Underlying mechanism for  $\varphi_0$ -JJs in MATBG.*—Next, based on the scattering matrix method [75, 76] and symmetry consideration, we show analytically that the valley-polarization and the warping effects of moiré bands are crucial in realizing a  $\varphi_0$ -JJ. As in the tight-binding model calculations above [40], we consider the case where the weak-link region is partially valley-polarized and conducting as schematically depicted in Fig. 1(b). In this case, we can linearize the momentum near the Fermi energy for each mode labeled by the transverse momentum  $k_y$  and the problem is reduced to a 1D scattering problem. For illustration, we demonstrate how the Andreev bound state associated with the  $k_y = 0$  mode (normal incident states), is affected by valley polarization and the warping terms. The 1D Hamiltonian is given by

nian associated with the  $k_y = 0$  mode can be written as  $H_{1D} = \sum_{\tau\alpha} \int dx \Psi_{\tau\alpha}^\dagger(x) \hat{H}_{\tau\alpha}(x) \Psi_{\tau\alpha}(x)$  [73]. Here,  $\tau = +/ -$  labels the valley index,  $\alpha = +/ -$  labels the incoming/outgoing normal states near Fermi energy,  $\Psi_{\tau\nu} = (\psi_{\tau\alpha}(x), \psi_{-\tau,-\alpha}^\dagger(x))^T$  denotes the Nambu basis, and

$$\hat{H}_{\tau\alpha}(x) = \begin{pmatrix} H_{N,\tau\alpha}(x) + \Delta_{vp}(x)\tau & \Delta_s(x) \\ \Delta_s(x) & H_{N,-\tau-\alpha}^*(x) + \Delta_{vp}(x)\tau \end{pmatrix}. \quad (3)$$

Here, the single-particle Hamiltonian  $H_N(x) = -i\hbar v_{f,\tau\alpha}(x)\partial_x + \Delta_{vp}(x)\tau$ , the longitudinal Fermi velocity along the current direction is given by  $v_{f,\tau\alpha}$  such that  $v_{f,\tau\alpha}(x) = v_{s,\tau\alpha}[\Theta(x) + \Theta(x-d)] + v_{vp,\tau\alpha}\theta(x)\Theta(d-x)$ , where  $v_{s,\tau\alpha}$  and  $v_{vp,\tau\alpha}$  are the Fermi velocities for the superconducting region and the valley-polarized weak-link region, respectively. Notably, the warping term which breaks the intravalley inversion symmetry could lead to  $v_{vp,\tau\alpha} \neq v_{vp,\tau-\alpha}$ . The superconducting pairing potential is written as  $\Delta_s(x) = \Delta_s(e^{i\frac{\phi}{2}}\Theta(-x) + e^{-i\frac{\phi}{2}}\Theta(x-d))$ , and the valley-polarized order parameter is  $\Delta_{vp}(x) = \Delta_{vp}\Theta(x)\Theta(d-x)$ .

With the effective one-dimensional Hamiltonian  $H_{1D}$ , we can solve the energies of the Andreev bound states  $\epsilon_\tau$  analytically ( $\tau$  is a good quantum number), which are related to the scattering matrices by [75, 76]

$$\text{Det}[1 - T_{LR}S_R T_{RL}S_L] = 0. \quad (4)$$

The scattering matrices  $S_{L(R)}$  and the transition matrices  $T_{RL}, T_{LR}$  can be obtained by matching the boundary conditions of scattering states at  $x = 0$  and  $x = d$  [73]. After inserting the scattering matrices into Eq. (S34), the energies of the Andreev bound states are given by [See SM[73]]

$$\cos(2\beta - \frac{2(\epsilon_\tau - \tau\Delta_{vp})}{E_T}) = \cos(\phi + \frac{\epsilon_\tau - \tau\Delta_{vp}}{\tau E_A}). \quad (5)$$

Here,  $\beta(\epsilon_\tau) = \arccos \frac{\epsilon_\tau}{\Delta_s}$ ,  $E_T = \hbar\bar{v}_{vp}/d$  is the Thouless energy,  $E_A = \hbar\delta\bar{v}_{vp}/d$  is an energy scale that reflects the intravalley asymmetry induced by the warping term, where  $\bar{v}_{vp}$  and  $\delta\bar{v}_{vp}$  are defined by  $\bar{v}_{vp} = 4(\sum_{\tau\alpha} v_{vp,\tau\alpha}^{-1})^{-1}$  and  $\delta\bar{v}_{vp} = 2(v_{vp,++}^{-1} + v_{vp,--}^{-1} - v_{vp,+-}^{-1} - v_{vp,-+}^{-1})^{-1}$ .

We then show that Eq. (5) can be used to explain many features of the numerical results of the tight-binding model as shown in Fig. 2. For example, we can calculate the Andreev bound state energies associated with the  $\tau = +/ -$  valleys by solving  $\epsilon_\tau(\phi)$  from Eq. (5) at  $\Delta_{vp}/\Delta_s = 0$  and  $\Delta_{vp}/\Delta_s = 1$  [see the gray lines and blue lines in Fig. 3(a), respectively]. Note that in Fig. 3(a), the valley degeneracy of Andreev bound states are lifted by the warping term and valley polarization. With the bound state energies  $\epsilon_\tau$ , it is straightforward to obtain the supercurrent  $I_s(\phi)$  by either using  $\frac{2e}{\hbar} \frac{\partial F_J(\phi)}{\partial \phi}$  or directly adopting the relation

$$I_s(\phi) = -\frac{2e}{\hbar} \sum_{\tau} \sum_{\epsilon_\tau > 0} \tanh(\frac{\epsilon_\tau}{2k_B T}) \frac{\partial \epsilon_\tau}{\partial \phi}. \quad (6)$$

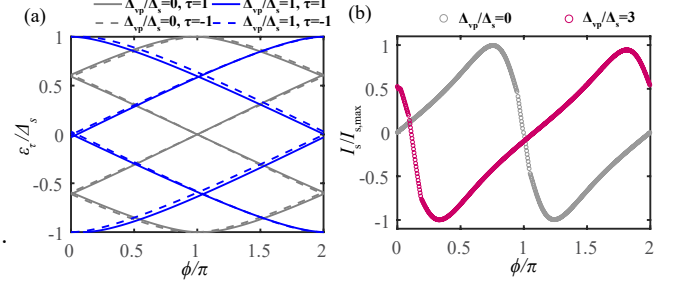


FIG. 3: (a) The energies of the Andreev bound states  $\epsilon_\tau$  versus the phase  $\phi$  obtained from Eq. (5) with  $\Delta_{vp}/\Delta_s = 0$  (gray lines) and  $\Delta_{vp}/\Delta_s = 1$  (blue lines), where  $\tau = \pm 1$  denotes the valley index. (b) The Josephson current  $I_s$  (normalized by its maximal value) versus  $\phi$  calculated with the Andreev bound states given by Eq. (5) with  $\Delta_{vp}/\Delta_s = 0$  (gray dots) and  $\Delta_{vp}/\Delta_s = 3$  (red dots), respectively. The two other energy scales are given by  $E_T = 0.65\Delta_s$  and  $E_A = 12\Delta_s$ , respectively.

As an illustration, we plot the calculated  $I_s(\phi)$  at the low temperature limit in the cases of  $\Delta_{vp}/\Delta_s = 0$  and  $\Delta_{vp}/\Delta_s = 3$  [see Fig. 3 (b)]. Notably, the features are in agreement with the ones shown in Figs. 2(d) and 2(e).

In the short junction and at the high temperature limit, we can obtain an analytical form for the Josephson current [73]:

$$I_s(\phi) \approx \frac{e\Delta_s^2}{2\hbar k_B T} \cos\left(\frac{2\Delta_{vp}}{E_T}\right) \sin(\phi - \varphi_0). \quad (7)$$

It can be seen that  $I_s(\phi)$  indeed significantly differs from the conventional form given by  $I_s(\phi) \propto \sin \phi$ . Specifically, the supercurrent exhibits a phase shift  $\varphi_0 = \Delta_{vp}/E_A$ , determining by both the valley polarization and Fermi velocity asymmetry induced by warping effects ( $\varphi_0 = 0$  if there is no this asymmetry as  $E_A \rightarrow \infty$ ). Remarkably, the factor  $\cos(\frac{2\Delta_{vp}}{E_T})$  indicates that the supercurrent oscillates periodically as a function of  $\Delta_{vp}$ , being consistent with the numerical result in Fig. 2(f). It is worth noting that the results are similar to Eq. 7 for modes with small transverse momentum  $k_y$  as well [73].

We now present a symmetry analysis to show why the valley polarization and the warping effects are crucial for the emergence of the  $\varphi_0$ -JJ in MATBG. Without these two ingredients, the system would exhibit time-reversal symmetry which gives  $I_{s,\tau}(\phi) \mapsto -I_{s,-\tau}(-\phi)$  and an intravalley inversion symmetry which gives  $I_{s,\tau}(\phi) \mapsto -I_{s,\tau}(-\phi)$ . As  $I_s(\phi) = \sum_{\tau} I_{s,\tau}(\phi)$ , it can be seen that both symmetries would enforce the total supercurrent to satisfy the condition  $I_s(\phi) = -I_s(-\phi)$ , so that  $I_s(\phi = 0) = 0$ . Therefore, the valley polarization together the warping effects would lift both the time-reversal symmetries and intravalley inversion symmetry so that the  $\varphi_0$ -JJ can be realized in the MATBG Josephson junctions. However, it is interesting to note that the  $\pi$ -junction [77–80] can still be induced by the valley polarization even without the warping terms, as the  $\cos(\frac{2\Delta_{vp}}{E_T})$  factor in Eq. (7) can be negative.

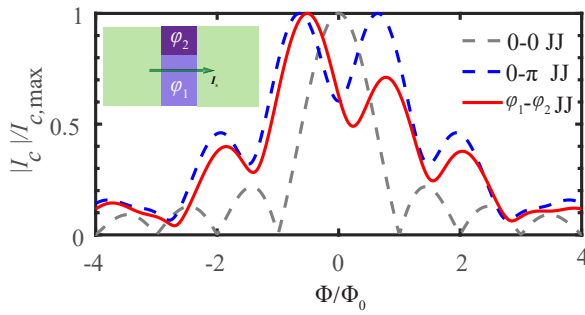


FIG. 4: The Fraunhofer patterns for different types of Josephson junctions. The critical current  $I_c$  (normalized by its maximal value) versus the magnetic flux  $\Phi$  passing through the junction (in units of  $\Phi_0 = h/2e$ ) for the 0-0 (gray), 0- $\pi$  (blue) and  $\varphi_1$ - $\varphi_2$  (red) Josesphson junctions respectively. The inset illustrates a simple two-domain model with different valley polarization induced phase shifts  $\varphi_1$  and  $\varphi_2$ . The Fraunhofer pattern of the  $\varphi_1$ - $\varphi_2$  junction matches the experimental observations well with  $\varphi_1 = 0.2$ ,  $\varphi_2 = \pi + 0.8$ . The widths of the  $\varphi_1$  and the  $\varphi_2$  sections are chosen to have the ratio  $W_{J1}/W_{J2} \approx 2.3$  [73].

*Possible connection to the observed unconventional Fraunhofer pattern.*—In practice, the sample inhomogeneity and the formations of valley polarization domain walls may lead the strength of  $\Delta_{vp}$  to be spatially non-uniform even inside the weak-link region [81]. One consequence is that the transport properties of the  $\varphi_0$ -JJ can be affected. As an illustration, we calculate the Fraunhofer pattern for a simple geometry with two valley polarization domains (see the inset of Fig. 4), in which each domain generates a phase difference of  $\varphi_1$  and  $\varphi_2$

respectively at the junction. Such a  $\varphi_1$ - $\varphi_2$  junction is a generalization of the previously studied 0- $\pi$  junctions [82–84]. Here, we plot the resulting Fraunhofer patterns in Fig. 4 and the details can be found in the SM [73]. Interestingly, the Fraunhofer pattern in this  $\varphi_1$ - $\varphi_2$  junction capture the main features found in the recent experiment [40] which exhibit a shift in the central peak, a large asymmetry with respect to the central peak, and a non-vanishing critical current as a function of magnetic fields. These features are not expected by conventional Josephson junctions nor 0- $\pi$  Josephson junctions [82–84].

*Discussion.*—Although we have considered the weak-link part of the junction to be partially polarized and conducting [40, 81], the conclusion that valley-polarized state induces  $\varphi_0$ -JJ is general according to our symmetry analysis. It applies even in the fully valley-polarized case, in which the state is usually topological insulating. As shown in the SM [73], we find that the  $\varphi_0$ -JJ behavior persists even when the valley-polarized state in the weak-link region is a fully gapped valley-polarized state with a Chern number two [20]. Note that in this case, the topologically protected edge states can play a role in mediating the Josephson current. Furthermore, our work can be easily extended to study the unconventional Josephson effects mediated by valley-polarized states in other moiré materials/superconductor heterostructures.

*Acknowledgments.*—The authors thank the discussions with Kin Fai Mak, Jaime Diez-Merida and Adrian Po. K.T.L. acknowledges the support of the Ministry of Science and Technology, China and the Hong Kong Research Grant Council through MOST20SC04, RFS2021-6S03, C6025-19G, AoE/P-701/20, 16310520, 16310219 and 16309718.

---

[1] R. Bistritzer and A. H. MacDonald, Proceedings of the National Academy of Sciences **108**, 12233 (2011).

[2] Y. Cao, V. Fatemi, A. Demir, S. Fang, S. L. Tomarken, J. Y. Luo, J. D. Sanchez-Yamagishi, K. Watanabe, T. Taniguchi, E. Kaxiras, R. C. Ashoori, and P. Jarillo-Herrero, Nature **556**, 80 (2018).

[3] Y. Cao, V. Fatemi, S. Fang, K. Watanabe, T. Taniguchi, E. Kaxiras, and P. Jarillo-Herrero, Nature **556**, 43 (2018).

[4] M. Koshino, N. F. Q. Yuan, T. Koretsune, M. Ochi, K. Kuroki, and L. Fu, Phys. Rev. X **8**, 031087 (2018).

[5] N. F. Q. Yuan and L. Fu, Phys. Rev. B **98**, 045103 (2018).

[6] H. Isobe, N. F. Q. Yuan, and L. Fu, Phys. Rev. X **8**, 041041 (2018).

[7] C.-C. Liu, L.-D. Zhang, W.-Q. Chen, and F. Yang, Phys. Rev. Lett. **121**, 217001 (2018).

[8] F. Wu, A. H. MacDonald, and I. Martin, Phys. Rev. Lett. **121**, 257001 (2018).

[9] C. Xu and L. Balents, Phys. Rev. Lett. **121**, 087001 (2018).

[10] B. Lian, Z. Wang, and B. A. Bernevig, Phys. Rev. Lett. **122**, 257002 (2019).

[11] Y. Jiang, X. Lai, K. Watanabe, T. Taniguchi, K. Haule, J. Mao, and E. Y. Andrei, Nature **573**, 91 (2019).

[12] J. González and T. Stauber, Phys. Rev. Lett. **122**, 026801 (2019).

[13] M. Yankowitz, S. Chen, H. Polshyn, Y. Zhang, K. Watanabe, T. Taniguchi, D. Graf, A. F. Young, and C. R. Dean, Science **363**, 1059 (2019).

[14] A. Kerelsky, L. J. McGilly, D. M. Kennes, L. Xian, M. Yankowitz, S. Chen, K. Watanabe, T. Taniguchi, J. Hone, C. Dean, A. Rubio, and A. N. Pasupathy, Nature **572**, 95 (2019).

[15] Y. Xie, B. Lian, B. Jäck, X. Liu, C.-L. Chiu, K. Watanabe, T. Taniguchi, B. A. Bernevig, and A. Yazdani, Nature **572**, 101 (2019).

[16] Y. Choi, J. Kemmer, Y. Peng, A. Thomson, H. Arora, R. Poliski, Y. Zhang, H. Ren, J. Alicea, G. Refael, F. von Oppen, K. Watanabe, T. Taniguchi, and S. Nadj-Perge, Nature Physics **15**, 1174 (2019).

[17] X. Lu, P. Stepanov, W. Yang, M. Xie, M. A. Aamir, I. Das, C. Urgell, K. Watanabe, T. Taniguchi, G. Zhang, A. Bachtold, A. H. MacDonald, and D. K. Efetov, Nature **574**, 653 (2019).

[18] A. L. Sharpe, E. J. Fox, A. W. Barnard, J. Finney, K. Watanabe, T. Taniguchi, M. A. Kastner, and D. Goldhaber-Gordon, *Science* **365**, 605 (2019).

[19] M. Serlin, C. L. Tschirhart, H. Polshyn, Y. Zhang, J. Zhu, K. Watanabe, T. Taniguchi, L. Balents, and A. F. Young, *Science* **367**, 900 (2020).

[20] P. Stepanov, I. Das, X. Lu, A. Fahimniya, K. Watanabe, T. Taniguchi, F. H. L. Koppens, J. Lischner, L. Levitov, and D. K. Efetov, *Nature* **583**, 375 (2020).

[21] D. Wong, K. P. Nuckolls, M. Oh, B. Lian, Y. Xie, S. Jeon, K. Watanabe, T. Taniguchi, B. A. Bernevig, and A. Yazdani, *Nature* **582**, 198 (2020).

[22] J. Kang and O. Vafek, *Phys. Rev. Lett.* **122**, 246401 (2019).

[23] Z. Song, Z. Wang, W. Shi, G. Li, C. Fang, and B. A. Bernevig, *Phys. Rev. Lett.* **123**, 036401 (2019).

[24] Y. Saito, J. Ge, K. Watanabe, T. Taniguchi, and A. F. Young, *Nature Physics* **16**, 926 (2020).

[25] U. Zondiner, A. Rozen, D. Rodan-Legrain, Y. Cao, R. Queiroz, T. Taniguchi, K. Watanabe, Y. Oreg, F. von Oppen, A. Stern, E. Berg, P. Jarillo-Herrero, and S. Ilani, *Nature* **582**, 203 (2020).

[26] Y. Choi, H. Kim, Y. Peng, A. Thomson, C. Lewandowski, R. Polski, Y. Zhang, H. S. Arora, K. Watanabe, T. Taniguchi, J. Alicea, and S. Nadj-Perge, *Nature* **589**, 536 (2021).

[27] Y.-T. Hsu, F. Wu, and S. Das Sarma, *Phys. Rev. B* **102**, 085103 (2020).

[28] H. C. Po, L. Zou, A. Vishwanath, and T. Senthil, *Phys. Rev. X* **8**, 031089 (2018).

[29] Y.-H. Zhang, D. Mao, Y. Cao, P. Jarillo-Herrero, and T. Senthil, *Phys. Rev. B* **99**, 075127 (2019).

[30] M. Xie and A. H. MacDonald, *Phys. Rev. Lett.* **124**, 097601 (2020).

[31] N. Bultinck, S. Chatterjee, and M. P. Zaletel, *Phys. Rev. Lett.* **124**, 166601 (2020).

[32] N. Bultinck, E. Khalaf, S. Liu, S. Chatterjee, A. Vishwanath, and M. P. Zaletel, *Phys. Rev. X* **10**, 031034 (2020).

[33] T. Cea and F. Guinea, *Phys. Rev. B* **102**, 045107 (2020).

[34] Y. Zhang, K. Jiang, Z. Wang, and F. Zhang, *Phys. Rev. B* **102**, 035136 (2020).

[35] J. Liu and X. Dai, *Phys. Rev. B* **103**, 035427 (2021).

[36] G. Shavit, E. Berg, A. Stern, and Y. Oreg, *arXiv e-prints* , arXiv:2107.08486 (2021), arXiv:2107.08486 [cond-mat.str-el] .

[37] Y. Cao, D. Rodan-Legrain, J. M. Park, N. F. Q. Yuan, K. Watanabe, T. Taniguchi, R. M. Fernandes, L. Fu, and P. Jarillo-Herrero, *Science* **372**, 264 (2021).

[38] D. Rodan-Legrain, Y. Cao, J. M. Park, S. C. de la Barrera, M. T. Randeria, K. Watanabe, T. Taniguchi, and P. Jarillo-Herrero, *Nature Nanotechnology* **16**, 769 (2021).

[39] F. K. de Vries, E. Portolés, G. Zheng, T. Taniguchi, K. Watanabe, T. Ihn, K. Ensslin, and P. Rickhaus, *Nature Nanotechnology* **16**, 760 (2021).

[40] J. Diez-Merida, A. Diez-Carlon, S. Y. Yang, Y. M. Xie, X. J. Gao, K. Watanabe, T. Taniguchi, X. Lu, K. T. Law, and D. K. Efetov, “Magnetic Josephson Junctions and Superconducting Diodes in Magic Angle Twisted Bilayer Graphene,” (2021), arXiv:2110.01067 [cond-mat.supr-con] .

[41] E. Portolés, S. Iwakiri, G. Zheng, P. Rickhaus, T. Taniguchi, K. Watanabe, T. Ihn, K. Ensslin, and F. K. de Vries, *arXiv e-prints* , arXiv:2201.13276 (2022), arXiv:2201.13276 [cond-mat.mes-hall] .

[42] C.-C. Tseng, X. Ma, Z. Liu, K. Watanabe, T. Taniguchi, J.-H. Chu, and M. Yankowitz, *arXiv e-prints* , arXiv:2202.01734 (2022), arXiv:2202.01734 .

[43] J. Linder and J. W. A. Robinson, *Nature Physics* **11**, 307 (2015).

[44] M. Eschrig, *Reports on Progress in Physics* **78**, 104501 (2015).

[45] L. B. Ioffe, V. B. Geshkenbein, M. V. Feigel'man, A. L. Fauchère, and G. Blatter, *Nature* **398**, 679 (1999).

[46] T. Yamashita, K. Tanikawa, S. Takahashi, and S. Maekawa, *Phys. Rev. Lett.* **95**, 097001 (2005).

[47] C. Padurariu and Y. V. Nazarov, *Phys. Rev. B* **81**, 144519 (2010).

[48] E. Strambini, A. Iorio, O. Durante, R. Citro, C. Sanz-Fernández, C. Guarcello, I. V. Tokatly, A. Braggio, M. Rocci, N. Ligato, V. Zannier, L. Sorba, F. S. Bergeret, and F. Giazotto, *Nature Nanotechnology* **15**, 656 (2020).

[49] F. S. Bergeret, A. F. Volkov, and K. B. Efetov, *Phys. Rev. Lett.* **86**, 4096 (2001).

[50] M. Eschrig, J. Kopu, J. C. Cuevas, and G. Schön, *Phys. Rev. Lett.* **90**, 137003 (2003).

[51] R. S. Keizer, S. T. B. Goennenwein, T. M. Klapwijk, G. Miao, G. Xiao, and A. Gupta, *Nature* **439**, 825 (2006).

[52] V. Braude and Y. V. Nazarov, *Phys. Rev. Lett.* **98**, 077003 (2007).

[53] A. V. Galaktionov, M. S. Kalenkov, and A. D. Zaikin, *Phys. Rev. B* **77**, 094520 (2008).

[54] M. Eschrig and T. Löfwander, *Nature Physics* **4**, 138 (2008).

[55] R. Grein, M. Eschrig, G. Metalidis, and G. Schön, *Phys. Rev. Lett.* **102**, 227005 (2009).

[56] B. Béri, J. N. Kupferschmidt, C. W. J. Beenakker, and P. W. Brouwer, *Phys. Rev. B* **79**, 024517 (2009).

[57] H. Enoksen, J. Linder, and A. Sudbø, *Phys. Rev. B* **85**, 014512 (2012).

[58] F. Konschelle and A. Buzdin, *Phys. Rev. Lett.* **102**, 017001 (2009).

[59] J.-F. Liu and K. S. Chan, *Phys. Rev. B* **82**, 184533 (2010).

[60] A. Buzdin, *Phys. Rev. Lett.* **101**, 107005 (2008).

[61] S. Mironov and A. Buzdin, *Phys. Rev. Lett.* **118**, 077001 (2017).

[62] A. A. Reynoso, G. Usaj, C. A. Balseiro, D. Feinberg, and M. Avignon, *Phys. Rev. Lett.* **101**, 107001 (2008).

[63] A. Zazunov, R. Egger, T. Jonckheere, and T. Martin, *Phys. Rev. Lett.* **103**, 147004 (2009).

[64] T. Yokoyama, M. Eto, and Y. V. Nazarov, *Phys. Rev. B* **89**, 195407 (2014).

[65] Y. Tanaka, T. Yokoyama, and N. Nagaosa, *Phys. Rev. Lett.* **103**, 107002 (2009).

[66] F. Dolcini, M. Houzet, and J. S. Meyer, *Phys. Rev. B* **92**, 035428 (2015).

[67] K. Sakurai, S. Ikegaya, and Y. Asano, *Phys. Rev. B* **96**, 224514 (2017).

[68] D. B. Szombati, S. Nadj-Perge, D. Car, S. R. Plissard, E. P. A. M. Bakkers, and L. P. Kouwenhoven, *Nature Physics* **12**, 568 (2016).

[69] A. Assouline, C. Feuillet-Palma, N. Bergeal, T. Zhang, A. Mottaghizadeh, A. Zimmers, E. Lhuillier, M. Eddrie, P. Atkinson, M. Aprili, and H. Aubin, *Nature Commun*

nlications **10**, 126 (2019).

[70] W. Mayer, M. C. Dartailh, J. Yuan, K. S. Wickramasinghe, E. Rossi, and J. Shabani, Nature Communications **11**, 212 (2020).

[71] F. Wu and S. Das Sarma, Phys. Rev. Lett. **124**, 046403 (2020).

[72] M. Oh, K. P. Nuckolls, D. Wong, R. L. Lee, X. Liu, K. Watanabe, T. Taniguchi, and A. Yazdani, Nature **600**, 240 (2021).

[73] See Supplementary Material for (i) trigonal warping effects of moiré bands and valley-polarized states, (ii) analytical calculations of the current-phase relation using the scattering matrix method, (iii) more details for the MATBG Josephson junction using the tight-binding method, (iv) the Magnetic interference for  $\varphi_0$ -Josephson junctions, (v) the  $\varphi_0$ -JJ beyond conventional pairings.

[74] M. Tinkham, *Introduction to superconductivity* (Courier Corporation, 2004).

[75] C. W. J. Beenakker, Phys. Rev. Lett. **67**, 3836 (1991).

[76] C. W. J. Beenakker, *Three “Universal” Mesoscopic Josephson Effects*. In: Fukuyama H., Ando T. (eds) *Transport Phenomena in Mesoscopic Systems* (Springer, 1992) pp. 235–253.

[77] V. V. Ryazanov, V. A. Oboznov, A. Y. Rusanov, A. V. Veretennikov, A. A. Golubov, and J. Aarts, Phys. Rev. Lett. **86**, 2427 (2001).

[78] T. Kontos, M. Aprili, J. Lesueur, and X. Grison, Phys. Rev. Lett. **86**, 304 (2001).

[79] A. A. Golubov, M. Y. Kupriyanov, and E. Il'ichev, Rev. Mod. Phys. **76**, 411 (2004).

[80] A. I. Buzdin, Rev. Mod. Phys. **77**, 935 (2005).

[81] S. Grover, M. Bocarsly, A. Uri, P. Stepanov, G. Di Battista, I. Roy, J. Xiao, A. Y. Meltzer, Y. Myasoedov, K. Pareek, K. Watanabe, T. Taniguchi, B. Yan, A. Stern, E. Berg, D. K. Efetov, and E. Zeldov, arXiv e-prints , arXiv:2201.06901 (2022).

[82] M. Weides, M. Kemmler, H. Kohlstedt, R. Waser, D. Koelle, R. Kleiner, and E. Goldobin, Phys. Rev. Lett. **97**, 247001 (2006).

[83] S. M. Frolov, D. J. Van Harlingen, V. V. Bolginov, V. A. Oboznov, and V. V. Ryazanov, Phys. Rev. B **74**, 020503 (2006).

[84] M. Kemmler, M. Weides, M. Weiler, M. Opel, S. T. B. Goennenwein, A. S. Vasenko, A. A. Golubov, H. Kohlstedt, D. Koelle, R. Kleiner, and E. Goldobin, Phys. Rev. B **81**, 054522 (2010).

# Supplementary Material for ‘Valley-Polarized State Induced $\varphi_0$ -Josephson Junction in Twisted Bilayer Graphene’

Ying-Ming Xie,<sup>1</sup> Dmitri K. Efetov<sup>2</sup>, K. T. Law<sup>1</sup>

<sup>1</sup>*Department of Physics, Hong Kong University of Science and Technology, Clear Water Bay, 999077 Hong Kong, China*

<sup>2</sup>*ICFO - Institut de Ciències Fotoniques, The Barcelona Institute of Science and Technology, Castelldefels, Barcelona, 08860, Spain*

## I. TRIGONAL WARPING EFFECTS OF MOIRÉ BANDS AND VALLEY-POLARIZED STATES

### A. Moiré bands of MATBG and trigonal warping effects

In the main text, the trigonal warping impact of moiré bands and its important effects on creating  $\varphi_0$ -Josephson junctions (JJs) in twisted bilayer graphene is highlighted. Here, we present the details of showing the trigonal warping effects using the continuum model of magic angle twisted bilayer graphene (MATBG) (which is depicted in Fig. S1(a)). The continuum model of MATBG (c.f. [1, 4]) can be written as

$$H_\tau(\mathbf{r}) = \begin{pmatrix} H_b(\mathbf{r}) & T(\mathbf{r}) \\ T^\dagger(\mathbf{r}) & H_t(\mathbf{r}) \end{pmatrix}. \quad (\text{S1})$$

Here, the intra-layer moiré Hamiltonian is

$$H_l = -\hbar v R(\theta)[(\hat{\mathbf{k}} - \mathbf{K}_\tau^{(l)}) \cdot (\tau \sigma_x, \sigma_y)] R^\dagger(\theta), \quad (\text{S2})$$

where  $\hbar v/a = 2.1354$  eV. Here,  $l = t/b$  and  $\tau = \pm$  label the top/bottom layers and  $\pm$  valleys respectively. The twist angle is denoted as  $\theta$ ,  $\sigma_j$  represent the Pauli matrices defined in the AB sublattice space,  $\mathbf{K}_\tau^{(l)}$  labels the Dirac point at valley  $\tau$  of the  $l$ -layer, and the rotational operator  $R(\theta) = \text{diag}(e^{-il\frac{\theta}{2}}, e^{il\frac{\theta}{2}})$ . The interlayer Hamiltonian  $T(\mathbf{r})$  can be written as

$$T(\mathbf{r}) = \begin{pmatrix} u & u' \\ u' & u \end{pmatrix} + \begin{pmatrix} u & u'e^{-i\omega_\tau} \\ u'e^{i\omega_\tau} & u \end{pmatrix} e^{-i\tau \mathbf{G}_2^M \cdot \mathbf{r}} + \begin{pmatrix} u & u'e^{i\omega_\tau} \\ u'e^{-i\omega_\tau} & u \end{pmatrix} e^{-i\tau \mathbf{G}_3^M \cdot \mathbf{r}}. \quad (\text{S3})$$

Here,  $\omega_\tau = \frac{2\pi}{3}\tau$ ,  $\mathbf{G}_i^M = \frac{4\pi}{\sqrt{3}L_M}(\cos \frac{(i-1)\pi}{3}, \sin \frac{(i-1)\pi}{3})$  with the moiré unit length  $L_M = a/\sin \theta \sim 14$  nm, and we adopt  $u = 0.0797$  eV,  $u' = 0.0975$  eV according to Ref. [4]. The moiré bands can be obtained by diagonalizing the continuum Hamiltonian using the plane wave basis  $\psi_{\mathbf{k}}(\mathbf{r}) = \sum_{\mathbf{G}} C_{\mathbf{G}} e^{i(\mathbf{k} + \mathbf{G}) \cdot \mathbf{r}}$  with  $G = n_1 \mathbf{G}_2^M + n_2 \mathbf{G}_3^M$ , where  $n_1, n_2$  are integers. Fig. S1(b) show the band structure of the lowest moiré bands near the charge neutrality point of MATBG [4].

To highlight the trigonal warping features of the moiré bands, a Fermi energy contour near half-filling of the  $\tau = +1$  valley (the black dashed line in Fig. S1(b)) is plotted in Fig. S1(c) (blue line). We can denote the warped Fermi energy contour as  $k_f(\varphi)$ . As  $k_f(\varphi) = k_f(\varphi + \frac{2\pi}{3})$  due to the  $C_3$  symmetry and an emergent  $C_{2x}$  symmetry in each valley such that  $k_f(\varphi) = k_f(-\varphi)$ . To the lowest order in  $\varphi$ , we can expand  $k_f(\varphi) \approx a + b \cos 3\varphi$ . By using  $a = 2.315$ ,  $b = -1.299$  (in unit of  $L_M^{-1}$ ), we find that  $k_f(\varphi)$  can approximately fit the warped Fermi energy contour of the continuum model. The Fermi energy contour at the  $\tau = -1$  valley can be obtained by a time-reversal operation.

Such prominent warping behaviour is a direct consequence of the narrow bandwidth and the constraint of  $D_3$  point group symmetry of MATBG [4, 5]. Here, we present the symmetry transformation properties under the generators of  $D_3$  which include a three-fold rotation along the  $z$ -axis and a two-fold rotation along the  $y$ -axis. Note that the moiré bands are assumed to be decoupled in the valley space so that only the terms that involve  $\tau_0$  and  $\tau_z$  are allowed. Without loss of generality, we consider the Fermi energy cuts the lower branch of the moiré bands only as shown in Fig. S1(b). In this case, we can construct a simple symmetry-invariant continuum model near  $\Gamma_m$  point as

$$H_{\text{eff}} = \lambda_0(k_x^2 + k_y^2) + \lambda_1 k_x(k_x^2 - 3k_y^2)\tau_z - \mu. \quad (\text{S4})$$

Here, the first term is the kinetic energy term,  $\mu$  denotes the chemical potential term, and the second term is the warping term which is opposite at the opposite valley to preserve the time-reversal symmetry  $T = \tau_x K$  and  $C_{2y} = \tau_x$  symmetry. The presence of the warping term breaks the intra-valley inversion symmetry as  $I_0 H_{\text{eff}}(\mathbf{k}) I_0^{-1} \neq H_{\text{eff}}(-\mathbf{k})$ ,

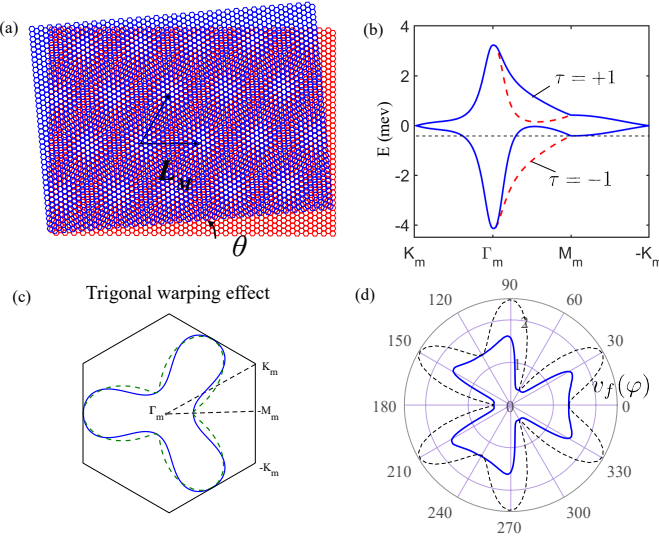


FIG. S1: (a) A schematic plot of the twisted bilayer graphene moiré superlattice ( $L_M$  is the lattice constant), which is formed using two layers of graphene with a small twisted angle  $\theta$ . (b) The lowest moiré bands of twisted bilayer graphene near charge neutrality points with the magic twist angle  $\theta = 1.05^\circ$ . The blue/red bands are from  $+K/-K$  valley ( $\tau = +1/\tau = -1$ ). Note that we have shifted the charge neutrality points to be at zero energy. (c) The Fermi contour (in blue) near half-filling [the black dashed line in (a)]. The green dashed line is plotted with  $k_f(\varphi) = a + b \cos 3\varphi$ . The black solid lines label the moiré Brillouin zone. (d) The blue line shows the anisotropic Fermi velocity along the radical direction  $v_f(\varphi)$ . The black lines are a plot of  $v_f(\varphi)$  estimated using  $k_f(\varphi)$ . The radius is in the unit of  $\text{meV}/\hbar L_M^{-1} \approx 2 \times 10^4 \text{ m/s}$ .

where under  $I_0 : \tau \mapsto \tau, \mathbf{k} \mapsto -\mathbf{k}$ . As emphasized in the main text, the breaking of intra-valley inversion symmetry together with the valley polarization enables the generation of  $\varphi_0$ -Josephson effect in MATBG even in the absence of the spin-orbit coupling.

One of the important consequences of the warping effects is to enable the velocity of incoming and outgoing states in the junction to be asymmetric, which plays a crucial role in creating a nontrivial  $\varphi_0$  as shown in later sections. To show the asymmetry of the Fermi velocity in the moiré bands, we plot the angular dependence of Fermi velocity  $v_f(\varphi)$  (see the blue line in Fig. S1(d), in unit of  $\text{meV}/\hbar L_M^{-1}$ ), which is defined as  $v_f(\varphi) = \sqrt{v_x(k_f(\varphi))^2 + v_y(k_f(\varphi))^2}$ ,  $k_f(\varphi)$  is the Fermi momentum contour as shown in Fig. S1(c). In other words,  $v_f(\varphi)$  is the Fermi velocity along the radical direction at each  $\varphi$ . For normal incident states, we can estimate the asymmetry of the Fermi velocity is given by  $v_f(\varphi = 0) - v_f(\varphi = \pi) \approx \text{meV}/\hbar L_M^{-1} \approx 2 \times 10^4 \text{ m/s}$ . Note that the Fermi velocity is two orders smaller than that of monolayer graphene due to the formation of flat bands under moiré superlattice potential.

To highlight the anisotropy of Fermi velocity induced by the warping term in Eq. (S4), we can rewrite the  $H_{\text{eff}}$  in polar coordinate as  $H_{\text{eff}}(k_r) = \lambda_0 k_r^2 + \lambda_1 k_r^3 \cos(3\varphi) \tau_z - \mu$ . For  $\tau = +1$  valley, the  $v_f(\varphi)$  can be obtained as  $v_f(\varphi) = \frac{\partial H_{\text{eff}}(k_f(\varphi))}{\partial k_r} = 2\lambda_0 k_f(\varphi) + 3\lambda_1 k_f^2(\varphi) \cos(3\varphi)$ . Inserting  $k_f(\varphi) \approx a + b \cos 3\varphi$ , the form of  $v_f(\varphi)$  is obtained. We made a plot of  $v_f(\varphi)$  with parameters  $\lambda_0 = 0.5347$  and  $\lambda_1 = 0.0885$  (see the dashed line in Fig. S1(d)). Although there is some deviation from the numerical one (in blue), all the symmetry features are captured. To obtain a closer fitting to the numerical results, one can expand it to higher order terms, which is not necessary for the purposes of this manuscript. Therefore, we have shown that the trigonal warping effects would result in anisotropic Fermi velocities. The warping term would induce an asymmetry for the velocities of the incoming and outgoing modes in our scattering matrix method calculations later.

## B. An illustration of valley-polarized states from the Hartree-Fock mean-field approximation

More detailed Hartree-Fock mean-field approximation for the moiré bands upon Coulomb interaction has been extensively studied in previous works. But for the sake of completeness and illustrate some features of the moiré bands upon the valley-polarization, we present the basic formalisms of the valley-polarized states from the Hartree-Fock approximation with a minimal interacting Hamiltonian:

$$H_0 = \sum_{\mathbf{k}, \tau, s} (\epsilon_{\mathbf{k}, \tau} - \mu) \psi_{\mathbf{k}, \tau, s}^\dagger \psi_{\mathbf{k}, \tau, s} + \frac{1}{2A} \sum_{\mathbf{q}} V_{\mathbf{q}} : \rho_{\mathbf{q}} \rho_{-\mathbf{q}} : . \quad (\text{S5})$$

Here,  $A$  is the sample area, the density operator,  $s$  denotes the spin index,  $\mu$  is the chemical potential for the single-particle moiré band,  $\rho_{\mathbf{q}} = \sum_{\mathbf{k}, \mathbf{k}', \tau, s} \langle c_{\mathbf{k}, \tau, s} | e^{i\mathbf{q} \cdot \mathbf{r}} | c_{\mathbf{k}', \tau, s} \rangle c_{\mathbf{k}, \tau}^\dagger c_{\mathbf{k}', \tau, s}$ . Without loss of generality, we focus on the first valence moiré band and the Coulomb interaction is projected to this moiré band [71]. The singlet-particle wave function can be decomposed into the plane wave basis as  $|c_{\mathbf{k}, \tau, s}\rangle = \frac{1}{\sqrt{A}} \sum_{\mathbf{G}} a_{\mathbf{k} + \mathbf{G}, \tau, s} e^{i(\mathbf{k} + \mathbf{G}) \cdot \mathbf{r}}$  with  $\mathbf{G}$  being the moiré reciprocal lattice vector.

The Hartree-Fock mean-field Hamiltonian with a spin- and valley-polarized ground state can be written as:

$$H_0^{HF} \approx \sum_{\mathbf{k}, \tau} E_{\mathbf{k}, \tau, s} \psi_{\mathbf{k}, \tau, s}^\dagger \psi_{\mathbf{k}, \tau, s}, \quad (S6)$$

where

$$E_{\mathbf{k}, \tau, s} = (\epsilon_{\mathbf{k}, \tau} - \mu) + \Delta_{\mathbf{k}, \tau, s}, \quad (S7)$$

$$\Delta_{\mathbf{k}, \tau, s} = \frac{1}{A} \sum_{\mathbf{k}', \tau', s'} V_{\mathbf{k}\mathbf{k}'\mathbf{k}'\mathbf{k}, ss's's'}^{\tau\tau'\tau'\tau} n_F(E_{\mathbf{k}', \tau', s'}) - \frac{1}{A} \sum_{\mathbf{k}'} V_{\mathbf{k}\mathbf{k}'\mathbf{k}\mathbf{k}', ssss}^{\tau\tau\tau\tau} n_F(E_{\mathbf{k}', \tau, s}). \quad (S8)$$

Here,  $n_F$  is the Fermi-Dirac occupation function, the first term of the right-hand of Eq. (S8) is the Hartree energy, while the second term is the Fock energy. The Coulomb interaction strength is written as

$$\begin{aligned} V_{\mathbf{k}_1 \mathbf{k}_2 \mathbf{k}_3 \mathbf{k}_4, ss's's}^{\tau\tau'\tau'\tau} &= \sum_{\mathbf{q}} V_{\mathbf{q}} \langle c_{\mathbf{k}_1, \tau, s} | e^{i\mathbf{q} \cdot \mathbf{r}} | c_{\mathbf{k}_4, \tau, s} \rangle \langle c_{\mathbf{k}_2, \tau', s'} | e^{-i\mathbf{q} \cdot \mathbf{r}} | c_{\mathbf{k}_3, \tau', s'} \rangle \\ &= \sum_{\mathbf{q}, \mathbf{G}_1, \mathbf{G}_2, \mathbf{G}_3, \mathbf{G}_4} V_{\mathbf{q}} a_{\mathbf{k}_1 + \mathbf{G}_1, \tau, s}^* a_{\mathbf{k}_2 + \mathbf{G}_2, \tau', s'}^* a_{\mathbf{k}_3 + \mathbf{G}_3, \tau', s'} a_{\mathbf{k}_4 + \mathbf{G}_4, \tau, s} \delta_{\mathbf{k}_1 + \mathbf{G}_1, \mathbf{q} + \mathbf{k}_4 + \mathbf{G}_4} \delta_{\mathbf{k}_3 + \mathbf{G}_3, \mathbf{q} + \mathbf{k}_2 + \mathbf{G}_2}. \end{aligned} \quad (S9)$$

Hence, the Coulomb interactions in the Hartree term and Fock term are written as

$$V_{\mathbf{k}\mathbf{k}'\mathbf{k}'\mathbf{k}, ss's's}^{\tau\tau'\tau'\tau} = \sum_{\mathbf{q}, \mathbf{G}_1, \mathbf{G}_2, \mathbf{G}_3, \mathbf{G}_4} V_{\mathbf{q}} a_{\mathbf{k} + \mathbf{G}_1, \tau, s}^* a_{\mathbf{k}' + \mathbf{G}_2, \tau', s'}^* a_{\mathbf{k}' + \mathbf{G}_3, \tau', s'} a_{\mathbf{k} + \mathbf{G}_4, \tau, s} \delta_{\mathbf{G}_1, \mathbf{q} + \mathbf{G}_4} \delta_{\mathbf{G}_3, \mathbf{q} + \mathbf{G}_2}, \quad (S10)$$

$$V_{\mathbf{k}\mathbf{k}'\mathbf{k}\mathbf{k}', ssss}^{\tau\tau\tau\tau} = \sum_{\mathbf{q}, \mathbf{G}_1, \mathbf{G}_2, \mathbf{G}_3, \mathbf{G}_4} V_{\mathbf{q}} a_{\mathbf{k} + \mathbf{G}_1, \tau, s}^* a_{\mathbf{k}' + \mathbf{G}_2, \tau, s}^* a_{\mathbf{k} + \mathbf{G}_3, \tau, s} a_{\mathbf{k}' + \mathbf{G}_4, \tau, s} \delta_{\mathbf{k} + \mathbf{G}_1, \mathbf{q} + \mathbf{k}' + \mathbf{G}_4} \delta_{\mathbf{k} + \mathbf{G}_3, \mathbf{q} + \mathbf{k}' + \mathbf{G}_2}. \quad (S11)$$

One can solve Eq. (S8) in a self-consistent way. Note that the doubly counted interacting energy should be subtracted after the mean-field approximation, which is given by

$$E_0 = \frac{1}{2A} \sum_{\mathbf{k}, \mathbf{k}', \tau, \tau', s, s'} [V_{\mathbf{k}\mathbf{k}'\mathbf{k}'\mathbf{k}, ss's's}^{\tau\tau'\tau'\tau} - V_{\mathbf{k}\mathbf{k}'\mathbf{k}\mathbf{k}', ssss}^{\tau\tau\tau\tau}] n_F(E_{\mathbf{k}, \tau, s}) n_F(E_{\mathbf{k}', \tau', s'}). \quad (S12)$$

Depending on the filling and the Coulomb interaction strength, various time-reversal breaking states with valley-polarization which satisfy the self-consistent Hartree-Fock equation can be obtained, including i) The fully valley-polarized, spin-unpolarized insulating or semi-metallic state. This state can appear when the Coulomb interaction strength is strong and the filling factor is near some integer fillings; ii) The partially valley-polarized, spin-unpolarized metallic states, which can appear when the Coulomb interactions are weaker [31]; and iii) The valley-polarized, spin-polarized states. A schematic illustration of the valley-polarized states is presented in the main text Fig. 1. As the focus of this work is the valley-polarized state, we neglect the spin polarization and rewrite the mean-field Hamiltonian as

$$H_0^{HF} \approx \sum_{\mathbf{k}, \tau} \psi_{\mathbf{k}, \tau}^\dagger [(\tilde{\epsilon}_{\mathbf{k}, \tau} - \mu) + \Delta_{\text{vp}, \mathbf{k}} \tau_z] \psi_{\mathbf{k}, \tau}, \quad (S13)$$

where  $\tilde{\epsilon}_{\mathbf{k}, \tau} = \epsilon_{\mathbf{k}, \tau} + (\Delta_{\mathbf{k}, \tau} + \Delta_{\mathbf{k}, -\tau})/2$  and  $\Delta_{\text{vp}, \mathbf{k}} = (\Delta_{\mathbf{k}, \tau} - \Delta_{\mathbf{k}, -\tau})/2$ , and  $\Delta_{\text{vp}} \tau_z$  is the valley-polarized order parameter. Note that here we are directly taking the valley-polarized state as the ansatz state. It is actually difficult to determine which state is more energetically favorable based on Hartree-Fock consideration alone. Especially when the correlated state appears at the weak-link region, the coupling with the superconducting regions can also be important.

## II. ANALYTICAL CALCULATIONS OF THE CURRENT-PHASE RELATION USING THE SCATTERING MATRIX METHOD

In the main text, we have used scattering matrix method to show that the studied MATBG Josephson junction is a  $\varphi_0$ -JJ and find that the valley polarization and warping effects are crucial in giving rise to the observed  $\varphi_0$ -JJ. As supplementary information, we present the corresponding details in this section.

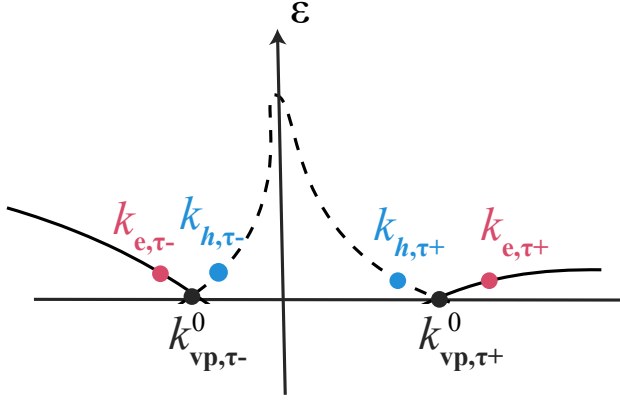


FIG. S2: A schematic plot of the wave vectors  $k_{e(h),\tau\alpha}$  on the quasi-particle excitation. The electron- and hole-like quasi-particle bands are highlighted with solid line and dashed line respectively.

### A. Model Hamiltonian

To gain some insight into the crucial features of the junction, we first look at the limit of  $\Delta_s, \Delta_{vp} \ll \mu$ , i.e., the bandwidth is the biggest energy scale. In this case, we can linearize the momentum near Fermi energy for a fixed transverse momentum  $k_y$  and obtain a low-energy effective model as

$$H = \frac{1}{2} \sum_{\tau\alpha} \sum_{k_y} \int dx \Psi_{k_y, \tau\alpha}^\dagger(x) \hat{H}_{k_y, \tau\alpha}(x) \Psi_{k_y, \tau\alpha}(x). \quad (\text{S14})$$

Here,  $\tau\pm$  labels the  $\pm K$  valley,  $\alpha = +/ -$  labels the incoming/outgoing normal states near Fermi energy,  $\Psi_{k_y, \tau\alpha} = (\psi_{k_y, \tau\alpha}(x), \psi_{k_y, -\tau, -\alpha}^\dagger(x))^T$  denotes the Nambu basis, and

$$\hat{H}_{\tau\alpha}(x) = \begin{pmatrix} -i\alpha\hbar v_{f, \tau\alpha}(k_y, x)\partial_x + \Delta_{vp}(x)\tau & \Delta_s(x) \\ \Delta_s(x) & i\alpha\hbar v_{f, -\tau, -\alpha}(k_y, x)\partial_x + \Delta_{vp}(x)\tau \end{pmatrix} \quad (\text{S15})$$

with the pairing potential  $\Delta_s(x) = \Delta_s(e^{i\frac{\phi}{2}}\theta(-x) + e^{-i\frac{\phi}{2}}\theta(x-d))$ , valley polarization  $\Delta_{vp}(x) = \Delta_{vp}\theta(x)\theta(d-x)$  (note that here, we have assumed a uniform valley polarization for the sake of simplicity), the longitudinal Fermi velocity at a fixed  $k_y$  of the superconducting part and junction part is given by  $v_{f, \tau\alpha}(k_y, x) = v_{s, \tau\alpha}(k_y)[\theta(x) + \theta(x-d)] + v_{vp, \tau\alpha}(k_y)\theta(x)\theta(d-x)$  (for the compact of notations, we will denote  $v_{f, \tau\alpha}(k_y, x) \equiv v_{f, \tau\alpha}(x)$  in the following). Here,  $\phi$  is the phase difference,  $d$  is the length of the junction,  $\Delta_{vp}$  is the valley polarization strength,  $v_{s, \tau\alpha}$ ,  $v_{f, \tau\alpha}$  are the longitudinal Fermi momentum along the current direction of the superconducting part and the junction part with valley polarization. One can verify that the whole Hamiltonian  $\hat{H}$  (dimension is eight by eight) preserves particle-hole symmetry  $P\hat{H}P^{-1} = -\hat{H}$  but breaks time-reversal symmetry:  $T\hat{H}T^{-1} \neq \hat{H}$  if  $\Delta_{vp}$  is finite. Here,  $\hat{P} = \rho_x \alpha_x \tau_x \hat{K}$ ,  $\hat{T} = \alpha_x \tau_x \hat{K}$  is complex conjugate, and  $\alpha_j$ ,  $\hat{K}$  is com  $\tau_j$ , and  $\rho_j$  are Pauli matrices defined in  $\alpha = +/ -$ , valley, and particle-hole space, respectively.

Note that in general  $v_{vp, \tau\alpha} \neq v_{vp, -\tau, -\alpha}$  due to the breaking of time-reversal symmetry, but  $v_{vp, \tau\alpha} \approx v_{vp, -\tau, -\alpha}$  in the limit of  $\Delta_{vp} \ll E_F'$ . On the other hand, the warping term breaking intra-valley time-reversal symmetry could lead to  $v_{vp, \tau\alpha} \neq v_{vp, \tau, -\alpha}$ , which plays a crucial role in giving rise to the  $\varphi_0$  junction as shown later.

It is worth noting that the model Hamiltonian resembles that for an S/F/S junction if the valley is regarded as a pseudo-spin (flips sign under both time-reversal and inversion operation). As we will show later, the  $\pi$  junction, which was commonly explored in S/F/S junctions, can also be stabilized in S/VP/S junctions. But we would emphasize that the physics system in our case is completely different, given that the polarization appears in valley degree of freedom rather than spin.

## B. Scattering states and boundary conditions

The scattering states in the S region of the left(L) and right(R) side are obtained as

$$\psi_{s,\tau\alpha}^L = \begin{pmatrix} e^{-i\alpha\beta} \\ e^{-i\frac{\phi}{2}} \end{pmatrix} e^{i\alpha k_{s,\tau\alpha}^0 x + \kappa_{\tau\alpha} x + ik_y y}, x \leq 0 \quad (\text{S16})$$

$$\psi_{s,\tau\alpha}^R = \begin{pmatrix} e^{i\alpha\beta} \\ e^{i\frac{\phi}{2}} \end{pmatrix} e^{i\alpha k_{s,\tau\alpha}^0 (x-L) - \kappa_{\tau\alpha} (x-L) + ik_y y}, x \geq d \quad (\text{S17})$$

with  $k_{s,\tau\alpha}^0$  being the Fermi momentum along the longitudinal direction for a fixed  $k_y$  and the definitions

$$\kappa_{\tau\alpha} = \frac{\sqrt{\Delta_s^2 - \epsilon^2}}{\hbar v_{s,\tau\alpha}}, \quad (\text{S18})$$

$$\beta = \begin{cases} \text{acos} \frac{\epsilon}{\Delta_s}, & \text{if } \epsilon < \Delta_s, \\ -i \text{acosh} \frac{\epsilon}{\Delta_s}, & \text{if } \epsilon > \Delta_s. \end{cases} \quad (\text{S19})$$

The in-gap states  $\psi_{s,\tau\alpha}^{L/R}$  with  $\epsilon \lesssim \Delta_s$  are superpositions of electron and hole with an exponential decay length  $\kappa_{\tau\alpha}^{-1}$  into the left/right superconducting regions. One can verify that the states in the S region possess time-reversal symmetry:  $\psi_s(\epsilon, -\phi) = \hat{T}\psi_s(\epsilon, \phi)$  with  $k_{s,\tau\alpha}^0 = k_{s,-\tau-\alpha}^0$ .

The scattering state in the VP region ( $0 \leq x \leq d$ ):

$$\psi_{vp,e,\tau\alpha} = \frac{1}{\sqrt{N_{e,\tau\alpha}}} \begin{pmatrix} 1 \\ 0 \end{pmatrix} e^{ik_{e,\tau\alpha} x + ik_y y}, \quad (\text{S20})$$

$$\psi_{vp,h,\tau\alpha} = \frac{1}{\sqrt{N_{h,\tau\alpha}}} \begin{pmatrix} 0 \\ 1 \end{pmatrix} e^{ik_{h,\tau\alpha} x + ik_y y}. \quad (\text{S21})$$

Here,  $k_{e,\tau\alpha}$  and  $k_{h,\tau\alpha}$  are the wave vectors for electron- and hole-like states, respectively [see an illustration in Fig. S2], and  $N_{e(h),\tau\alpha}$  are normalization factors to ensure that the scattering matrices are unitary. Up to the leading order,  $k_{e,\tau\alpha} \approx \alpha k_{vp,\tau\alpha}^0 + \delta k_{e,\tau\alpha}$ ,  $k_{h,\tau\alpha} \approx \alpha k_{vp,\tau\alpha}^0 + \delta k_{h,\tau\alpha}$  with

$$\delta k_{e,\tau\alpha} = \frac{\epsilon - \tau \Delta_{\text{vp}}}{\alpha \hbar v_{vp,\tau\alpha}}, \quad (\text{S22})$$

$$\delta k_{h,\tau\alpha} = -\frac{\epsilon - \tau \Delta_{\text{vp}}}{\alpha \hbar v_{vp,-\tau-\alpha}}. \quad (\text{S23})$$

Here,  $\psi_{vp,e,\tau+}$ ,  $\psi_{vp,h,\tau-}$  are the states moving in the  $+x$  direction, while  $\psi_{vp,e,\tau-}$ ,  $\psi_{vp,h,\tau+}$  are the states moving in the  $-x$  direction. The particle-hole symmetry requires  $\psi_{vp,h}(-\epsilon) = \hat{P}\psi_{vp,e}(\epsilon)$  so that  $\delta k_{h,\tau\alpha}(-\epsilon) = -\delta k_{e,-\tau-\alpha}(\epsilon)$ . The factors  $\sqrt{N_{e,\tau\alpha}}$  and  $\sqrt{N_{h,\tau\alpha}}$  are to ensure that the scattering matrix is unitary.

As  $\hat{H}$  is block-diagonalized in the valley space with  $[\tau_z, \hat{H}] = 0$ , we can solve the scattering matrix for  $\tau = +$  and  $\tau = -$  separately. We also assume that the transverse momentum  $k_y$  is conserved during the scatterings. The boundary conditions at  $x = 0$  and  $x = d$  are:

$$a\psi_{s,\tau+}^L(x=0) + b\psi_{s,\tau-}^L(x=0) = c_e^+ \psi_{vp,e,\tau+}(x=0) + c_e^- \psi_{vp,e,\tau-}(x=0) + c_h^+ \psi_{vp,h,\tau+}(x=0) + c_h^- \psi_{vp,h,\tau-}(x=0), \quad (\text{S24})$$

$$a'\psi_{s,\tau+}^R(x=d) + b'\psi_{s,\tau-}^R(x=d) = c_e^+ \psi_{vp,e,\tau+}(x=d) + c_e^- \psi_{vp,e,\tau-}(x=d) + c_h^+ \psi_{vp,h,\tau+}(x=d) + c_h^- \psi_{vp,h,\tau-}(x=d), \quad (\text{S25})$$

$$av_{s,\tau+} \psi_{s,\tau+}^L(x=0) + bv_{s,\tau-} \psi_{s,\tau-}^L(x=0) = v_{vp,\tau+} c_e^+ \psi_{vp,e,\tau+}(x=0) - v_{vp,\tau-} c_e^- \psi_{vp,e,\tau-}(x=0) + v_{vp,-\tau-} c_h^+ \psi_{vp,h,\tau+}(x=0) - v_{vp,-\tau+} c_h^- \psi_{vp,h,\tau-}(x=0), \quad (\text{S26})$$

$$a'v_{s,\tau+} k_{0,\tau+} \psi_{s,\tau+}^R(x=d) - b'v_{s,\tau-} \psi_{s,\tau-}^R(x=d) = v_{vp,\tau+} c_e^+ \psi_{vp,e,\tau+}(x=d) - v_{vp,\tau-} c_e^- \psi_{vp,e,\tau-}(x=d) + v_{vp,-\tau-} c_h^+ \psi_{vp,h,\tau+}(x=d) - v_{vp,-\tau+} c_h^- \psi_{vp,h,\tau-}(x=d). \quad (\text{S27})$$

Here, Eqs. (S24) and (S25) are obtained from the continuity of wavefunction, while Eqs. (S26) and (S27) are obtained from the conservation of particle current, which for each state is given by  $\text{Im}(\langle \psi | \frac{\partial H_{\tau\alpha}(\mathbf{r})}{\partial p_x} | \psi \rangle) = \langle \psi | \text{diag}(\alpha v_{f,\tau\alpha}, -\alpha v_{f,-\tau-\alpha}) | \psi \rangle$ .

### C. Andreev bound states in the case without normal reflections

We now solve the Andreev bound states using the scattering matrix method [75, 76]. First, we need to work out the scattering matrices. We can define

$$a(L) = a, b(L) = b, a(R) = a', b(R) = b'; \quad (\text{S28})$$

$$c_e^\dagger(L) = c_e^+, c_e^-(L) = c_e^-, c_h^\dagger(L) = c_h^+, c_h^-(L) = c_h^-; \quad (\text{S29})$$

$$c_e^\dagger(R) = c_e^+ e^{i(k_{e,\tau+} + \delta k_{e,\tau+})d}, c_e^-(R) = c_e^- e^{i(k_{e,\tau-} + \delta k_{e,\tau-})d}, \quad (\text{S30})$$

$$c_h^\dagger(R) = c_h^+ e^{i(k_{h,\tau+} + \delta k_{h,\tau+})d}, c_h^-(R) = c_h^- e^{i(k_{h,\tau-} + \delta k_{h,\tau-})d}. \quad (\text{S31})$$

The scattering matrices in the scattering method are defined as

$$\begin{pmatrix} c_e^+(L) \\ c_h^-(L) \end{pmatrix} = S_L \begin{pmatrix} c_e^-(L) \\ c_h^+(L) \end{pmatrix}, \begin{pmatrix} c_e^-(R) \\ c_h^+(R) \end{pmatrix} = S_R \begin{pmatrix} c_e^+(R) \\ c_h^-(R) \end{pmatrix}, \quad (\text{S32})$$

and the transition matrices are defined as

$$\begin{pmatrix} c_e^+(R) \\ c_h^-(R) \end{pmatrix} = T_{RL} \begin{pmatrix} c_e^+(L) \\ c_h^-(L) \end{pmatrix}, \begin{pmatrix} c_e^-(L) \\ c_h^+(L) \end{pmatrix} = T_{LR} \begin{pmatrix} c_e^-(R) \\ c_h^+(R) \end{pmatrix}. \quad (\text{S33})$$

According to the scattering matrix method [75, 76], the energies of Andreev bound states are given by

$$\text{Det}[1 - T_{LR} S_R T_{RL} S_L] = 0. \quad (\text{S34})$$

The transmission matrices can be directly obtained according to the definitions Eqs. (S28) to (S31) and Eq. S33 as

$$T_{RL} = \begin{pmatrix} e^{i(k_{e,\tau+}^0 + \delta k_{e,\tau+})d} & 0 \\ 0 & e^{i(k_{h,\tau-}^0 + \delta k_{h,\tau-})d} \end{pmatrix}, \quad (\text{S35})$$

$$T_{LR} = \begin{pmatrix} e^{-i(k_{e,\tau-}^0 + \delta k_{e,\tau-})d} & 0 \\ 0 & e^{-i(k_{h,\tau+}^0 + \delta k_{h,\tau+})d} \end{pmatrix}. \quad (\text{S36})$$

The form of scattering matrix  $S_{L(R)}$  would depend on the interface at  $x = 0$  and  $x = d$ . Let us first consider the case without chemical potential difference between the superconducting region and valley polarized region, i.e.,  $\mu = \mu'$ . In this case,  $v_{vp,\tau\pm} = v_{s,\tau\pm}$ , the factors in the scattering states can be simply taken as  $N_{e,\tau\alpha} = N_{h,\tau\alpha} = 1$ . Using the definitions Eqs. (S28) to (S31) and the boundary conditions Eqs. (S24) to (S27), one can easily obtain

$$S_{L(R)} = \begin{pmatrix} 0 & e^{\pm i\frac{\phi}{2} - i\beta} \\ e^{\mp i\frac{\phi}{2} - i\beta} & 0 \end{pmatrix}. \quad (\text{S37})$$

Here,  $\beta = \text{acos}\frac{\epsilon_\tau}{\Delta_s}$  for in-gap Andreev bound states, and only Andreev reflections in the scattering matrix are finite due to the absence of momentum mismatches. By inserting the scattering matrix back to Eq. (S34), we find that the energies of Andreev bound states are given by

$$\cos(2\beta - \frac{2(\epsilon_\tau - \tau\Delta_{vp})d}{\hbar\bar{v}_{vp}}) = \cos(\phi + \frac{(\epsilon_\tau - \tau\Delta_{vp})d}{\tau\hbar\delta v_{vp}}), \quad (\text{S38})$$

where

$$\bar{v}_{vp} = \frac{4}{\sum_{\tau\alpha} v_{vp,\tau\alpha}^{-1}}, \delta\bar{v}_{vp} = \frac{2}{v_{vp,++}^{-1} + v_{vp,--}^{-1} - v_{vp,+-}^{-1} - v_{vp,-+}^{-1}}. \quad (\text{S39})$$

We can further define two energy scales: one is the Thouless energy  $E_T = \hbar\bar{v}_{vp}/d$ , and the other one is  $E_A = \hbar\delta\bar{v}_{vp}/d$ , which reflects the intra-valley asymmetry induced by the warping term. Then Eq. S38 is rewritten as

$$\cos(2\beta - \frac{2(\epsilon_\tau - \tau\Delta_{vp})}{E_T}) = \cos(\phi + \frac{\epsilon_\tau - \tau\Delta_{vp}}{\tau E_A}). \quad (\text{S40})$$

It clearly shows that the phase  $\phi$  is shifted as  $\tilde{\phi} = \phi - \varphi_0$  with  $\varphi_0 = \Delta_{vp}/E_A$  due to the combination of valley polarization and warping effects. As we will see later,  $\varphi_0$  would manifest as the phase shift in a current-phase relation, which would result in the so-called  $\varphi_0$  junction. In the short junction limit,  $\epsilon \ll E_A, E_T$ , we can actually obtain the energies of the bound states:

$$\epsilon_\tau = \Delta_s \sqrt{1 - \sin^2(\frac{\tilde{\phi}}{2} - \frac{\tau\Delta_{vp}}{E_T})}. \quad (\text{S41})$$

#### D. Andreev bound states in the case with normal reflections

In general, the chemical potential between the superconducting region and valley-polarized region is different with  $\mu \neq \mu'$ . To see the effects of such a difference in chemical potential, we solved the scattering matrices in the same way as

$$S_{L(R)} = \begin{pmatrix} r_N & r_A e^{\pm i \frac{\phi}{2} - i\beta} \\ r_A e^{\mp i \frac{\phi}{2} - i\beta} & r_N \end{pmatrix} \quad (\text{S42})$$

with

$$r_A = e^{i\beta} X^{-1} (v_{vp,\tau+} + v_{vp,\tau-})(v_{s,\tau+} + v_{s,\tau-}), \quad (\text{S43})$$

$$r_N = 2iX^{-1} \sin \beta \sqrt{(v_{vp,\tau+} + v_{s,\tau-})(v_{vp,\tau-} + v_{s,\tau+})(v_{vp,\tau+} - v_{s,\tau+})(v_{vp,\tau-} - v_{s,\tau-})}, \quad (\text{S44})$$

$$X = e^{i\beta} (v_{vp,\tau+} + v_{s,\tau-})(v_{vp,\tau-} + v_{s,\tau+}) - e^{-i\beta} (v_{vp,\tau+} - v_{s,\tau+})(v_{vp,\tau-} - v_{s,\tau-}). \quad (\text{S45})$$

Here,  $r_A, r_N$  are coefficients for Andreev reflections and normal reflections. Note that we have used  $N_{e,\tau+} = N_{h,\tau+} = \sqrt{(v_{vp,\tau+} - v_{s,\tau+})(v_{vp,\tau+} + v_{s,\tau+})}$ ,  $N_{e,\tau-} = N_{h,\tau-} = \sqrt{(v_{vp,\tau-} - v_{s,\tau-})(v_{vp,\tau-} + v_{s,\tau-})}$ . One can verify that the scattering matrix is unitary with  $|r_A|^2 + |r_N|^2 = 1$  for the in-gap bound states with  $\epsilon < \Delta$ . Evidently, the normal reflections  $r_N$  would be finite due to the momentum mismatches, i.e.,  $v_{vp,\tau\pm} \neq v_{s,\tau\pm}$  induced by the difference in the chemical potential ( $\mu \neq \mu'$ ). It can also be seen that the scattering matrix Eq. (S42) would return to the Eq. (S37) if there is no momentum mismatch.

Next, we solve the energies of Andreev bound states in the case of finite normal reflections. For the compact of notations, we rewrite the scattering matrix as:

$$S_{L(R)} = \begin{pmatrix} ie^{i\eta} & \sqrt{1-r^2} e^{i\eta} \\ \sqrt{1-r^2} e^{i\eta} & ie^{i\eta} \end{pmatrix}. \quad (\text{S46})$$

Here,  $r = |r_N|$ ,  $\eta = \text{Arg}[X^{-1}]$ . By substituting the scattering back to Eq. (S34), we find that the Andreev bound states are given by

$$\cos\left(2\eta + \frac{2(\epsilon - \tau\Delta_{\text{vp}})}{E_T}\right) + r^2 \cos\left(\sum_{\alpha} k_{\tau\alpha}^0 d\right) = (1 - r^2) \cos\left(\phi + \frac{\epsilon - \tau\Delta_{\text{vp}}}{\tau E_A}\right) \quad (\text{S47})$$

As expected, the phase shift  $\varphi_0 = \frac{\Delta_{\text{vp}}}{E_A}$  would not be affected by the presence of normal reflections. Instead, the normal reflection would mainly weaken the magnitude of the supercurrent and thus is not essential for our study.

#### E. Free energy and Josephson currents

The free energy of a JJ can be written as

$$F = \int d\mathbf{r} \frac{|\Delta_s|^2}{U} - \frac{1}{\beta} \sum_{\epsilon_n} \ln(1 + e^{-\beta\epsilon_n}), \quad (\text{S48})$$

where  $\epsilon_n$  is the eigenenergies of the BdG Hamiltonian of the Josephson junction,  $\beta = 1/k_B T$ ,  $U$  is an effective interaction strength. One can further subtract a constant normal state free energy  $F(\Delta_s = 0)$  to avoid the divergence at large energies and would not affect the current-phase relation  $I_s(\phi)$  [76]. The supercurrent through the JJ can be obtained from the free energy with

$$I_s(\phi) = \frac{2e}{\hbar} \frac{\partial F}{\partial \phi} = \frac{2e}{\hbar} \sum_{\epsilon_n} \frac{1}{e^{\beta\epsilon_n} + 1} \frac{\partial \epsilon_n}{\partial \phi} = -\frac{2e}{\hbar} \sum_{\epsilon_n > 0} \tanh\left(\frac{\beta\epsilon_n}{2}\right) \frac{\partial \epsilon_n}{\partial \phi}. \quad (\text{S49})$$

Here,  $e$  is the charge of an electron. One can easily figure out the current units by using  $\hbar \approx 6.581 \times 10^{-13}$  meV·s and  $e/s \approx 1.6 \times 10^{-19}$  A (A is Ampere), i.e.,  $2e/\hbar \approx 486$  nA/meV.

By substituting the bound state energy Eq. (S41) into Eq. (S49), and at the high temperature limit  $\Delta_s/k_B T \ll 1$ , we obtain Eq. (7) of the main text:

$$I_s(\phi) \approx \frac{e\Delta_s^2}{2\hbar k_B T} \cos\left(\frac{2\Delta_{\text{vp}}}{E_T}\right) \sin\left(\phi - \frac{\Delta_{\text{vp}}}{E_A}\right). \quad (\text{S50})$$

## F. The scattering modes of different transverse momentum $k_y$

In the previous sections, we have solved the 1D scattering matrix problem for each mode at a fixed  $k_y$ . To obtain the total supercurrent through the junction, we need to insert different longitudinal Fermi momentum  $v_{f,\tau\alpha}(k_y)$ , and sum over different  $k_y$  that are quantized by the finite width. Unfortunately, we could not do it analytically due to the complicated warping effects. For the completeness, we still present a brief discussion of the effects of  $k_y$  here.

The total supercurrent through this Josephson junction is given by

$$I_s(\phi) = \sum_{k_y} I_{s,k_y}(\phi). \quad (\text{S51})$$

In the short junction and at the high temperature limit, the supercurrent at a phase difference  $\phi$ :  $I_{s,k_y}(\phi)$  carried by each mode can be obtained by replacing  $E_T$ ,  $E_A$  in Eq. (S50) with the ones calculated from  $v_{f,\tau\alpha}(k_y)$ . As shown in Fig. S1(d), the value of longitudinal Fermi momentum  $v_{f,\tau\alpha}(k_y)$  and its asymmetry near  $k_y = 0$  are similar so that the resulting current-phase relation is expected to be similar to Eq. (S50) for a small transverse momentum. However, the situation becomes complicated in the large transverse momentum  $k_y$ . Because of the warping effects, there are multiple scattering modes near Fermi energy for a fixed  $k_y$  [see Figs. S1(c) and S1(d)], which are not captured by Hamiltonian (S15) that only includes one incoming electron- or hole-dominant mode. Nevertheless, we expect the scattering modes with large momentum to carry less supercurrent and thus in the main text, we find that the 1D scattering Hamiltonian provides a good understanding of our numerical results, in which the current carried by all incoming modes are included.

## III. MORE DETAILS FOR THE MATBG JOSEPHSON JUNCTION USING THE TIGHT-BINDING METHOD

In this section, we present more details about the numerical calculations, including the geometry details, the result in the case of turning off the warping effects, and the result in the case of the weak-link region being a half-filling valley-polarized Chern insulator with a Chern number two.

### A. Model and Geometry details

As introduced in the main text, we adopt the following effective tight-binding model to capture MATBG Josephson junction:

$$H_{\text{eff}} = \sum_{\langle ij \rangle, \xi} t_1 c_{i\xi}^\dagger c_{j\xi} + \sum_{\langle ij \rangle', \xi} t_{2\xi} c_{i\xi}^\dagger c_{j\xi} + \text{H.c.} - \sum_{i, \xi} \mu_i c_{i\xi}^\dagger c_{i\xi} + \sum_{i \in (L, R), \xi} (\Delta_s e^{i\phi_{L(R)}} c_{i\xi}^\dagger c_{i-\xi}^\dagger + \text{H.c.}) + \sum_{i \in M, \xi} \Delta_{\text{vp}} c_{i\xi}^\dagger (\tau_z)_{\xi\xi'} c_{i\xi}. \quad (\text{S52})$$

See the main text for the detailed definitions of the ingredients in Hamiltonian  $H_{\text{eff}}$ . Here, we depict the adopted geometry of the MATBG Josephson junction in Fig. S3. The superconducting order parameter  $\Delta_s$  and valley-polarized order parameter  $\Delta_{\text{vp}}$  are added in the green region and gray region of the top panel of Fig. S3, respectively. As shown in the bottom panel of Fig. S3, the lowest moiré bands near the charge neutrality are captured by hoppings on the two-orbital hexagonal lattice in each region, where  $t_1$  represents the first-nearest hopping,  $t_2$  represents the complex fifth-nearest hopping (giving rise to the warping effects). We note that the minimal tight-binding model proposed in Ref. [4] that is used to capture the moiré bands up to the lowest hopping is narrower than that from the continuum model shown in Fig. S1(b). This however would not affect our result as the presence of  $\varphi_0$ -JJs is determined by the symmetries according to our main text analysis. The key length scales are also highlighted in Fig. S3. The lattice sites in Fig. S3 label the center of wannier orbitals so that the length of the nearest bonds is the moiré lattice constant  $L_M$ . We thus measure the adopted junction length  $d$  and  $W$  in main text in units of  $L_M$ .

### B. The case without warping effects

In the main text, the warping effects are naturally included in our calculations with the fifth-nearest hopping  $t_{2\xi} \neq 0$  (c.f. [4, 5]). As discussed in the main text, the warping term would lift the intra-valley inversion symmetry so that the

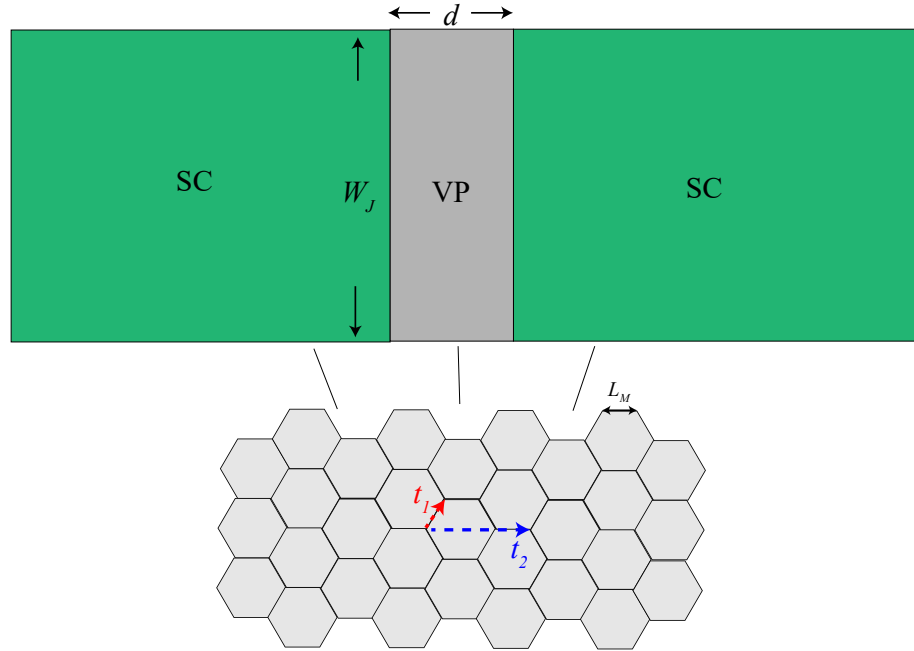


FIG. S3: The top panel presents the junction geometry that is adopted in the evaluation of Josephson supercurrent through the JJ using the effective tight-binding model  $H$  (Eq. (S52)).  $d$  and  $W_J$  represent the junction length and width, respectively. Here SC, VP represents the region with superconductivity and valley polarization. The bottom panel shows a hexagonal lattice used in the tight-binding model calculation, where  $t_1$  denotes the first-nearest hopping,  $t_2$  denotes the complex fifth-nearest hopping (resulting in warping term) in  $H$ , and the length of the nearest bond is  $L_M$ .

minimal free energy of the junction is not necessary 0- or  $\pi$ -JJ, resulting in a  $\varphi_0$ -JJ in general. To make a comparison, we now artificially turn off the warping term. As expected, we find that the junction is restricted to be 0- or  $\pi$ -JJ [Fig. S4(a)]. We consistently find that the anomalous Josephson current, i.e.,  $J_s(\phi = 0)$ , vanishes [Fig. S4(b)]. It thus clearly shows that the warping effects are crucial for the ground state of MATBG Josephson junction to be  $\varphi_0$ -JJ, which is in agreement with our symmetry analysis presented in the main text.

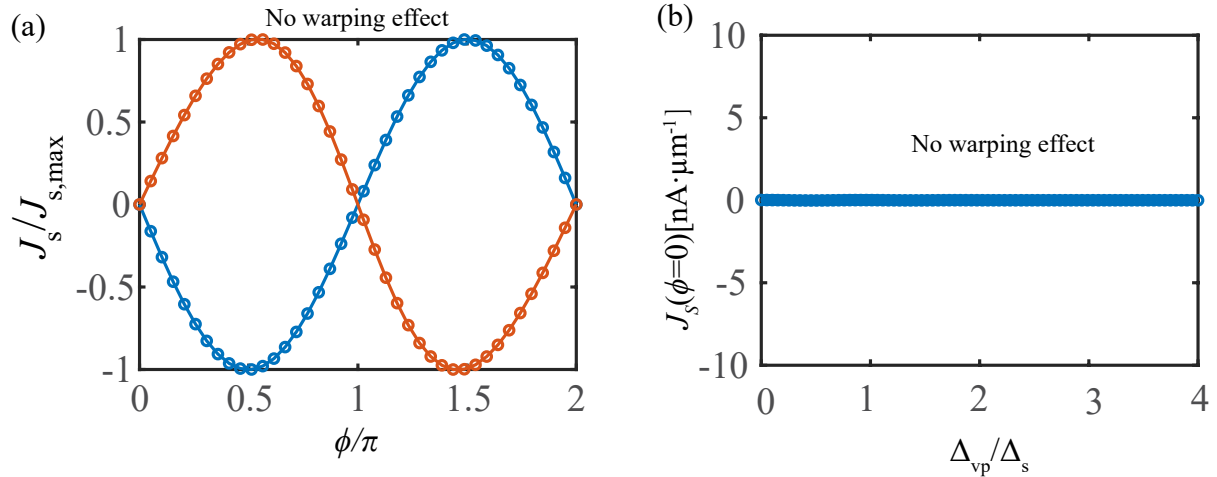


FIG. S4: The current-phase relation and vanishing of anomalous Josephson current in the case without warping effects. (a) Typical curves of Josephson current (normalized by its maximal value) versus Josephson phase difference  $\phi$  of the MATBG Josephson junction when the warping term is turned off ( $t_{2\xi} = 0$ ), which can only display 0- or  $\pi$ -junction behavior. (b) The anomalous Josephson current vanishes for various valley polarization strengths where warping effects are not included.

### C. The case with junction region being valley-polarized Chern insulating states

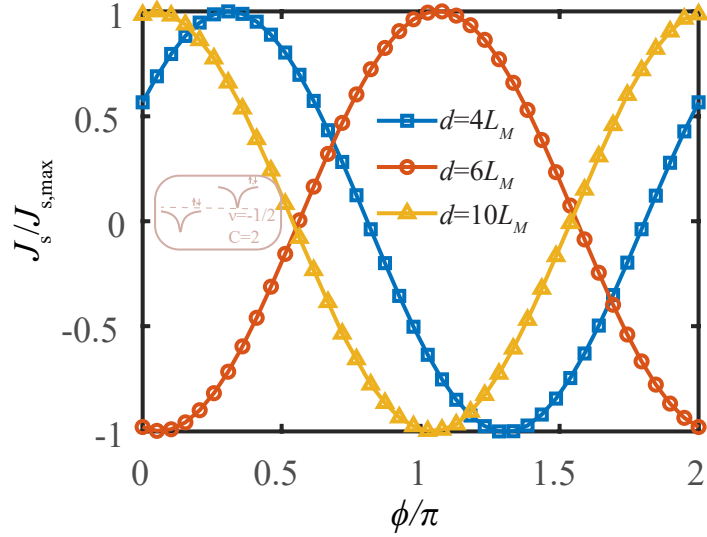


FIG. S5: The supercurrent density  $J_s$  (normalized by its maximal value) versus the phase difference  $\phi$  with junction length  $d = 4L_M, 6L_M, 10L_M$ , where the junction region is set to be the valley-polarized Chern insulating states with  $C = 2$  at half-filling that are illustrated with a schematic inset plot. Here we set the temperature  $T = 0.05T_c$ .

It was pointed out in the main text that the mechanism: valley-polarized state mediates unconventional Josephson junction is quite robust regardless of whether the state is topologically trivial or nontrivial. In this section, as a demonstration, we present the calculated current-phase relation [Fig. S5] by setting the junction region to be half-filling ( $\nu = -1/2$ ) valley-polarized Chern insulating states with Chern number  $C = 2$  [see a schematic illustration in the inset of Fig. S5]. One can add a Haldane term to the tight-binding Hamiltonian (S52) in order to make the junction region topological (c.f. Ref. [40]). In this case, as shown in Fig. S5, the curves of supercurrent  $J_s$  (normalized by its maximal value) versus the phase difference  $\phi$  would still display a finite phase shift, i.e.,  $\sin(\phi - \varphi_0)$ , for various junction lengths  $d$ . In other words, the junction would still behave a  $\varphi_0$ -JJ. Note that in the topological case, the edge states that can mediate some supercurrents may play an additional role. Nevertheless, Fig. S5 clearly shows that our conclusion about the valley polarization causing  $\varphi_0$ -JJ is not affected. It is understandable given that time-reversal and intra-valley inversion symmetry are still broken by the valley-polarized Chern bands in this case.

## IV. THE MAGNETIC INTERFERENCE FOR $\varphi_0$ -JOSEPHSON JUNCTIONS

### A. The magnetic interference of a uniform $\varphi_0$ Josephson junction-standard Fraunhofer pattern

In this section, we show that the magnetic interference of a uniform  $\varphi_0$  Josephson junction should be the standard Fraunhofer pattern. The gauge invariant phase difference across an extended junction is

$$\gamma = \tilde{\phi} + \frac{2e}{\hbar} \int \mathbf{A} \cdot d\mathbf{l} \quad (S53)$$

with  $\tilde{\phi} = \phi - \varphi_0$ ,  $\varphi_0$  denoting the phase shift in  $\varphi_0$ -junction. For an out of plane magnetic field, the gauge can be chosen as  $\mathbf{A} = (-By, 0)$ . The Josephson current is given by

$$I_s = \int dy j(\mathbf{r}, \tilde{\phi} - \frac{2e}{\hbar} \int_{-d/2}^{d/2} dx By). \quad (S54)$$

Assuming that the current follows the simplest  $\sin(\phi - \varphi_0)$  feature, we will obtain

$$I_s = \int_{-W_J/2}^{W_J/2} dy j(y) \sin(\tilde{\phi} - \frac{2e}{\hbar} Byd).$$

Here, we denote the width of the junction to be  $W_J$ . In the case of a uniform current density  $j(x) = j_b$ , then

$$I_s(\Phi) = \frac{j_b \sin \tilde{\phi} \sin(\pi\Phi/\Phi_0)}{\frac{\pi}{\Phi_0} BL}, \quad (\text{S55})$$

where the flux quantum  $\Phi_0 = h/2e$ ,  $\Phi = B \times W_J d$ . Thus,

$$I_c(\Phi) = I_c \left| \frac{\sin(\pi\Phi/\Phi_0)}{\pi\Phi/\Phi_0} \right|, \quad (\text{S56})$$

where the critical current at zero-field is denoted as  $I_c = j_0 W_J$ . Hence, for a uniform  $\varphi_0$  JJ, our phenomenological calculation suggests that the critical current as a function of external fields  $I_c(\Phi)$  follows the standard Fraunhofer pattern.

## B. Phenomenological theory for the magnetic interference of a $\varphi_1$ - $\varphi_2$ Josephson junction

As we have mentioned in the main text, the total current through this junction under external magnetic fields can be written as

$$I_s(\phi) = \int_{-W_{J1}}^0 dy j_b \sin(\phi - \varphi_1 - \frac{2e}{\hbar} Byd) + \int_0^{W_{J2}} dy j_b \sin(\phi - \varphi_2 - \frac{2e}{\hbar} Byd). \quad (\text{S57})$$

Note that  $\varphi_1$  and  $\varphi_2$  would be different as  $\Delta_{\text{vp}}$  in two domain walls are different. If  $\varphi_1 = 0$  and  $\varphi_2 = \pi$ , the scenario would reduce to the 0- $\pi$  JJ studied in Ref. [82–84], where the Fraunhofer pattern exhibits a dip near the zero magnetic flux due to the cancellation of the supercurrent of the 0-JJ parts and  $\pi$ -JJ parts. In our case, the  $\varphi_1$  and  $\varphi_2$  can be a value ranging from 0 to  $2\pi$  due to the formation of  $\varphi_0$ -JJ. Hence, we call it  $\varphi_1$ - $\varphi_2$  JJ.

The Fraunhofer pattern of the  $\varphi_1$ - $\varphi_2$  JJ can be obtained from Eq. (S57). Specifically, the total supercurrent is written as

$$I_s(\phi) = \frac{I_{s1}}{2\pi\frac{\Phi_1}{\Phi_0}} (\cos(\phi - \varphi_1) - \cos(\phi - \varphi_1 + 2\pi\frac{\Phi_1}{\Phi_0})) + \frac{I_{s2}}{2\pi\frac{\Phi_2}{\Phi_0}} (\cos(\phi - \varphi_2 - 2\pi\frac{\Phi_2}{\Phi_0}) - \cos(\phi - \varphi_2)). \quad (\text{S58})$$

Here,  $I_{s1} = j_b W_{J1}$  and  $I_{s2} = j_b W_{J2}$  denote the current through the two domain walls, respectively, and the magnetic flux though the  $j$ -th domain wall is  $\Phi_j = B W_j d$ . For the sake of simplicity, we denote  $I_{s1} = \frac{1}{2}(1+\delta)I_s$ ,  $I_{s2} = \frac{1}{2}(1-\delta)I_s$ ,  $\Phi_1 = \frac{1}{2}(1+\delta)\Phi$ , and  $\Phi_2 = \frac{1}{2}(1-\delta)\Phi$ , where  $I_s = I_{s1} + I_{s2}$  is the total supercurrent through the junction, and  $\Phi = B(W_{J1} + W_{J2})d$  is the total magnetic flux. Using these notations, the

$$I_s(\phi) = \frac{I_s}{\frac{2\pi\Phi}{\Phi_0}} [\cos(\phi - \varphi_1) - \cos(\phi - \varphi_2) + \cos(\phi - \varphi_2 - \frac{\pi(1-\delta)\Phi}{\Phi_0}) - \cos(\phi - \varphi_1 + \frac{\pi(1+\delta)\Phi}{\Phi_0})] \quad (\text{S59})$$

$$= \frac{I_s}{\frac{\pi\Phi}{\Phi_0}} [\sin(\phi - \frac{\varphi_+}{2} + \delta\frac{\pi\Phi}{\Phi_0}) \sin(\frac{\varphi_-}{2} + \frac{\pi\Phi}{\Phi_0}) - \sin(\phi - \frac{\varphi_+}{2}) \sin(\frac{\varphi_-}{2})], \quad (\text{S60})$$

where  $\varphi_{\pm} = \varphi_2 \pm \varphi_1$ .

The critical current  $I_c = \max(I_s(\phi))$ , given by the maximal value of  $I_s(\phi)$  within  $0 \leq \phi \leq 2\pi$ . For the 0-0 JJ, one can easily obtain the standard Fraunhofer pattern  $I_c(\Phi) = I_s \left| \frac{\sin(\pi\Phi/\Phi_0)}{\pi\Phi/\Phi_0} \right|$ . Due to the presence of the asymmetry parameter  $\delta$ , beyond 0-0 JJ, we could only find analytical solutions of the critical current in some special cases, such as in the limit of  $\delta = 0$ :

$$I_c(\Phi) = I_s \left| \frac{\sin(\frac{\varphi_-}{2} + \frac{\pi\Phi}{\Phi_0}) - \sin(\frac{\varphi_-}{2})}{\frac{\pi\Phi}{\Phi_0}} \right|. \quad (\text{S61})$$

It can be noted that the critical current is always zero if the magnetic flux reaches certain integer flux quantum  $\Phi = 2n\Phi_0$  ( $n$  are finite integers). As there is no node in the Fraunhofer pattern of experiments, we remove these nodes by introducing a finite asymmetric parameter  $\delta$ . For example, at  $\Phi = 2n\Phi_0$ , the critical current becomes  $I_s \left| \frac{\sin(\frac{\varphi_-}{2}) \sin \delta n \pi}{2n\pi} \right|$ , which could be finite if  $\delta \neq 0$ .

It is worth noting that another key feature of the experimentally observed Fraunhofer pattern is to exhibit the  $I_c(\Phi) \neq I_c(-\Phi)$ . In the cases of 0-0 JJ and 0- $\pi$  JJ, we find that the resulting Fraunhofer patterns are always symmetric,

regardless of the choice of  $\delta$ . However, if we consider  $\varphi_0$ -JJ, where  $\varphi_{\pm}$  can take a more generic value rather than 0 or  $\pi$ , we find that the resulting Fraunhofer pattern is asymmetric in general. In Fig. 4 of the main text, we plotted the Fraunhofer pattern for the 0-0 JJ, 0- $\pi$  JJ, and  $\varphi_1$ - $\varphi_2$  JJ with  $\delta = 0.4$ ,  $\varphi_1 = 0.2$ ,  $\varphi_2 = \pi + 0.8$ . The resulting Fraunhofer pattern arising from  $\varphi_1$ - $\varphi_2$  JJ is quite consistent with that seen in the experiment. Our calculation thus suggests that the presence of  $\varphi_0$ -JJs could provide a plausible explanation for such highly unconventional Fraunhofer patterns.

### C. Detection of $\varphi_0$ -JJ with a superconducting MATBG SQUID

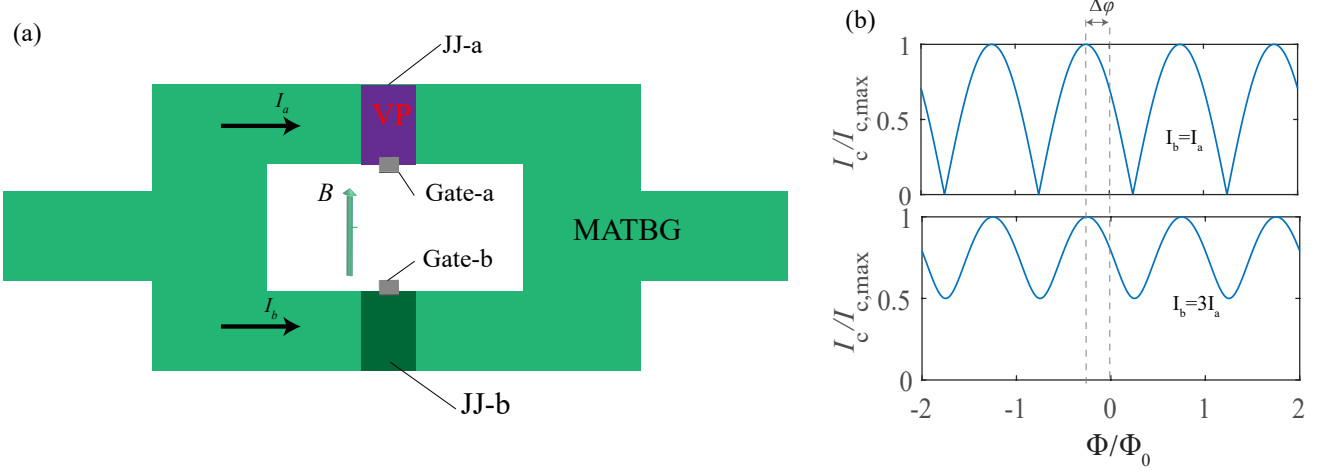


FIG. S6: (a) A schematic plot of a MATBG SQUID. Here, JJ-a represents a junction region controlled by gate-a, while JJ-b represents the other junction region controlled by gate-b.  $B$  is an out of plane magnetic field. (b) The critical supercurrent (normalized by its maximal value) as a function of the magnetic flux  $\Phi$  in the case of  $I_b = I_a$  (top panel),  $I_b = 3I_a$  (bottom panel).  $I_a$ ,  $I_b$  are the supercurrent through JJ-a, JJ-b, respectively. The phase shift of the interference pattern  $\Delta\varphi$  is highlighted.

The SQUID can be used to identify the  $\varphi_0$ -JJ behavior in the experiments [68]. For the sake of completeness, as shown in Fig. S6(a), here we propose a MATBG SQUID geometry to detect the  $\varphi_0$ -JJ predicted by our theory. In this geometry, there are two weak-linked junction regions that are achieved by local gates-a,b. Without loss of generality, we consider one is the  $\varphi_0$ -JJ with the junction gated into valley-polarized states (JJ-a), while the other one is the conventional JJ (JJ-b).

The total supercurrent through the SQUID under magnetic fields is written as

$$I_s = I_b \sin(\phi_b) + I_a \sin(\phi_a - \varphi_0) \quad (\text{S62})$$

with

$$\varphi_b - \varphi_a = 2\pi\Phi/\Phi_0. \quad (\text{S63})$$

Here,  $I_a(\varphi_a)$  and  $I_b(\varphi_b)$  are the supercurrent (phase difference) across the JJ-a, JJ-b, respectively.  $\Phi$  is the magnetic flux through the SQUID. In a simple case where  $I_a = I_b = I_0$ , we can obtain the critical current at each magnetic flux as

$$I_c = 2I_0 \left| \cos\left(\pi \frac{\Phi}{\Phi_0} + \frac{\varphi_0}{2}\right) \right|. \quad (\text{S64})$$

Hence, the  $\varphi_0$  would cause a phase shift in the SQUID pattern [see the top panel of Fig. S6(b)], where  $\Delta\varphi = \varphi_0/2\pi$ . In general,  $I_a$  and  $I_b$  are not equal. As a illustration, we plot the magnetic interference pattern with  $I_b = 3I_a$  in Fig. S6(c). In this case, it can be seen that although the critical currents no longer vanish at certain magnetic fields, the phase shift does not change.

Therefore, the proposed MATBG SQUID provides a feasible way to directly measure the predicted  $\varphi_0$  phase shift. Upon finishing our work, we noticed that the MATBG SQUID geometry has recently been successfully fabricated in the experiment [41]. Our work thus would motive experimentalists to further gate the junction region into valley-polarized states and study the proposed unconventional Josephson effects in the near future.

## V. THE $\varphi_0$ -JJ BEYOND CONVENTIONAL PAIRINGS

Supplementary Table 1: Classifications of all possible momentum independent pairing of TBG according to the irreducible representations of the  $D_3$  symmetry group.

IRs	$A_1$	$A_2$	$E$
$C_{3z} = \tau_0 \otimes e^{-i\frac{\pi}{3}\sigma_z}$	+1	+1	+2
$C_{2y} = \tau_x \otimes i\sigma_y$	+1	+1	0
Spin-singlet	$\tau_x \otimes i\sigma_y$	—	—
Spin-triplet	$i\tau_y \otimes \sigma_x$	—	$(i\tau_y \otimes \sigma_z, i\tau_y \otimes \sigma_0)$

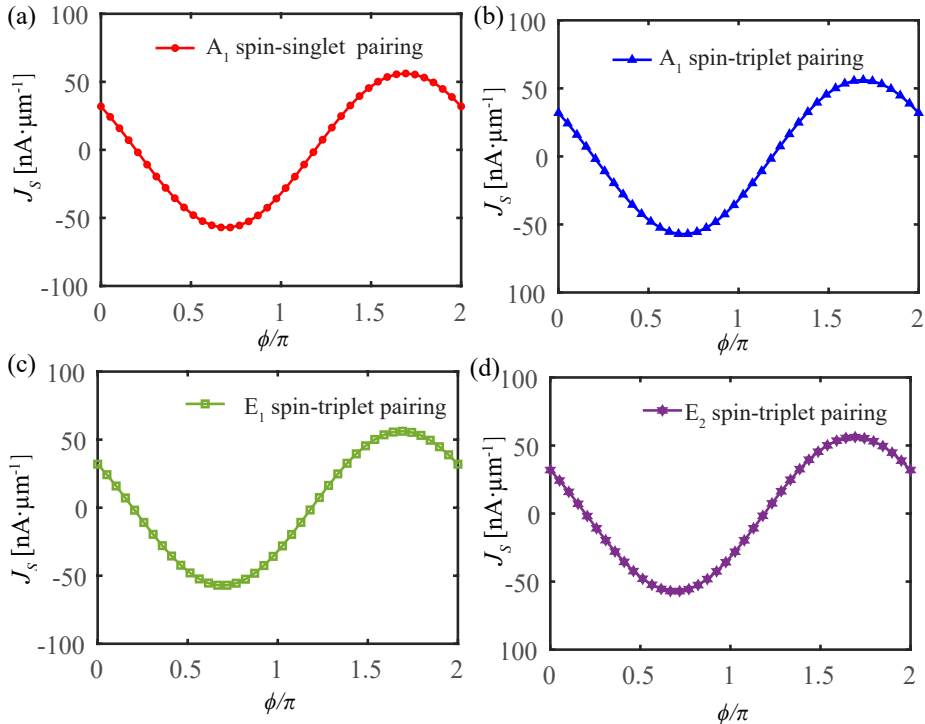


FIG. S7: (a)-(d) The supercurrent density  $J_s$  (in the unit of  $\text{nA} \cdot \mu\text{m}^{-1}$ ) versus the Josephson phase difference  $\phi$  for  $A_1$  spin-singlet pairing,  $A_1$  spin-triplet pairings,  $E_1$  spin-triplet pairing,  $E_2$  spin-triplet pairing, respectively. Here we adopt a valley polarization strength  $\Delta_{\text{vp}}/\Delta_s = 3$  and a temperature  $T/T_c = 0.3$ .

In the main text, to be specific, we have adopted the spin-singlet pairing as the pairing order parameter for the superconducting part of the MATBG Josephson junction. In this section, we point out that the  $\varphi_0$ -JJ can still persist even when the pairing is unconventional, such as various spin-triplet pairings. The pairings can be expanded in the space formed by spin and valley degrees of freedom. We first classify the possible pairings using irreducible representations of the  $D_3$  crystal group of MATBG. For simplicity, we focus on all  $\mathbf{k}$ -independent inter-valley pairings.

Specifically, the generators of  $D_3$  point contains a three-fold rotation along the  $z$ -axis represented by  $C_{3z} = \tau_0 \otimes e^{-i\frac{\pi}{3}\sigma_z}$ , and a two-fold rotation along the  $y$ -axis represented by  $C_{2y} = \tau_x \otimes i\sigma_y$ . Here,  $\sigma$  and  $\tau$  are Pauli matrices defined in spin- and valley-space. Note that  $C_{2y}$  would exchange the  $K$  and  $-K$  valley, while  $C_3$  would not.

The pairing matrix transforms under the a point group symmetry operation as:

$$g\hat{\Delta}_s \mapsto U^\dagger(g)\hat{\Delta}_s U^*(g), \quad (\text{S65})$$

where  $\hat{\Delta}_s$  is defined in Nambu basis:  $(\psi_{+,\uparrow}, \psi_{+,\downarrow}, \psi_{-,\uparrow}, \psi_{-,\downarrow})^T$  with  $+/-$  as valley index and  $\uparrow/\downarrow$  for spin up/spin down,  $U(g)$  is the matrix representation of the generator  $g$  in the spin- and valley-space. Note that  $\hat{\Delta}_s = -\hat{\Delta}_s^T$  due to the Fermi statistics, and the representation of  $\hat{\Delta}_s$  in the valley degree of freedom is restricted to be  $\tau_x$  and  $\tau_y$ , i.e., inter-valley nature. All the  $\mathbf{k}$ -independent inter-valley pairings are summarized in Table 1.

There is one inter-valley spin-singlet  $A_1$  pairing :  $\Delta_{A_1,s} = \tau_x \otimes i\sigma_y$ ,, and there are two inter-valley spin-triplet pairings: one one-dimensional spin-triplet  $A_1$ -pairing  $\Delta_{A_1,t} = i\tau_y \otimes \sigma_x$ , and one two-dimensional spin-triplet  $E$ -pairing, which we label as  $E_1$ -pairing and  $E_2$ -pairing with  $(\Delta_{E,1}, \Delta_{E,2}) = (i\tau_y \otimes \sigma_z, i\tau_y \otimes \sigma_0)$ . Note that the pairings labeled by different irreducible representations do not mix, and the mixing of  $\Delta_{A_1,s}$  and  $\Delta_{A_1,t}$  is expected to be neglectable as the spin-orbit coupling in graphene is extremely small. It is also worth noting that the possible nematic pairings can be constructed using the pairing matrices in the two-dimensional  $E$ -pairing.

We can replace the order parameter of the superconducting part with the above unconventional uniform pairings in the previous tight-binding model calculation and evaluate the supercurrent in the same way. As shown in Figs. S7 (a)-(d), we find that the current-phase relation is unchanged in the cases of various spin-triplet pairings, which thus implies that our result is not sensitive to the spin configurations of Cooper pairs of the superconducting part. This observation is understandable as the appearance of  $\varphi_0$ -JJ is mainly induced by the valley polarization of the junction region.